Master's thesis

NTNU
Norwegian University of Science and Technology
Faculty of Natural Sciences
Department of Materials Science and Engineering

Sunniva Meltzer

Predicting phase transitions and rotational dynamics in the plastic crystals $[(CH_3)_4N][FeCl_4]$ and $[(CH_3)_4N][FeBr_4]$ by using *ab initio* molecular dynamics with machine learned force fields

Master's thesis in Nanotechnology
Supervisor: Benjamin A. D. Williamson
Co-supervisor: Sverre M. Selbach and Julian Walker
June 2023

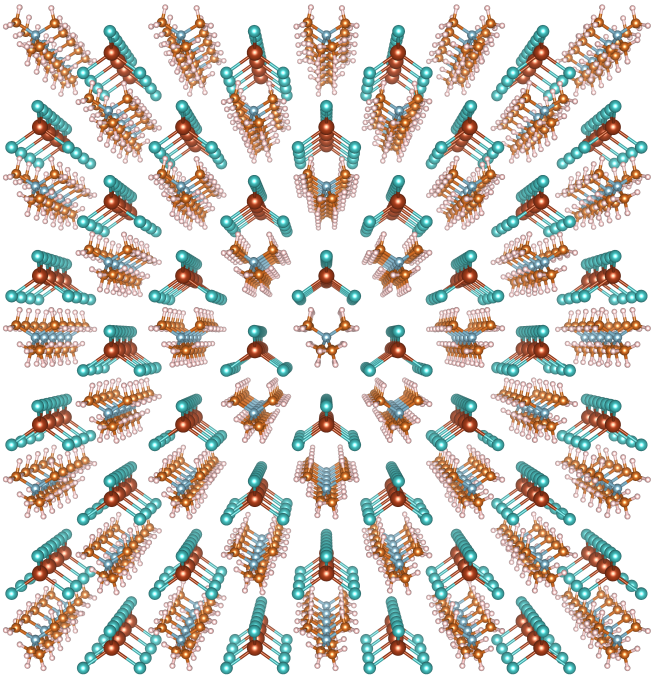

NTNU
Norwegian University of
Science and Technology

Sunniva Meltzer

Predicting phase transitions and rotational dynamics in the plastic crystals $[(CH_3)_4N][FeCl_4]$ and $[(CH_3)_4N][FeBr_4]$ by using *ab initio* molecular dynamics with machine learned force fields

Master's thesis in Nanotechnology
Supervisor: Benjamin A. D. Williamson
Co-supervisor: Sverre M. Selbach and Julian Walker
June 2023

Norwegian University of Science and Technology
Faculty of Natural Sciences
Department of Materials Science and Engineering

NTNU
Norwegian University of
Science and Technology

IN THIS short historical survey, I hope to give, to the best of my ability, the early experimental evidence concerning plastic crystals, and I apologize in advance if there remain some important gaps in my text, since I am a specialist in the study of physical properties of organic compounds, but am not so learned, either in inorganic chemistry or in theoretical physics.

— J. Timmermans [1]

PREFACE

This master's thesis is written as part of the subject *TMT4910 Nanotechnology, Master's Thesis* at the Department of Materials Science and Engineering at the Norwegian University of Science and Technology (NTNU), as a continuation of the project work carried out in the subject *TMT4510 Nanotechnology, specialisation course* [2]. All calculations were performed on resources provided by UNINETT Sigma2 - the National Infrastructure for High Performance Computing and Data Storage in Norway.

ACKNOWLEDGEMENTS

First and foremost I want to give my biggest thanks to my supervisors, Dr. Benjamin A. D. Williamson, Prof. Sverre M. Selbach and Assoc. Prof. Julian Walker for their help and guidance throughout this project work. Without them, this thesis would not have been possible. A special thank you to Ben for his close follow-up, for always being available and providing detailed instructions for all the VASP calculations, in addition to sharing Jupyter Notebooks and helping me gain a deeper insight in the analytic work.

I would also like to thank the FACET group for their weekly meetings, providing a platform for sharing results and discussing interesting research questions.

Last, but not least, I would like to thank my family for their continuous support, and for proofreading this thesis. I also want to thank all my friends in Trondheim for making these five years at NTNU the best of my life. A special thanks to Gunvor and Kasper for for all the conversations, walks and support during good and challenging periods.

Sunniva Meltzer
June 19, 2023

ABSTRACT

Plastic crystals are a novel class of materials that exhibit excellent piezoelectric and ferroelectric properties, in addition to being soft and flexible due to rotational freedom of the molecules. This makes them promising candidates for replacing lead-based ferroelectrics in the metal oxide ceramics industry, being a sustainable, recyclable and cheap alternative. In addition, plastic crystals can potentially be used for thermal energy storage applications and to improve the ionic conductivity in Li-ion batteries. However, plastic crystals are poorly understood on a microscopic level, and are challenging to model since the rotational freedom of the molecules makes them highly disordered.

The aim of this thesis was to predict the phase transitions and study the rotational dynamics in the plastic crystals tetramethylammonium irontetrachloride ($[(CH_3)_4N][FeCl_4]$) and tetramethylammonium irontetrabromide ($[(CH_3)_4N][FeBr_4]$) through *ab initio* molecular dynamics simulations using machine learned force fields. The phase transitions were studied by investigating the change in lattice parameters, unit cell volume and XRD spectra for the two compounds upon heating and cooling from 200 K to 400 K and back again, and the rotational dynamics were studied by analysing the autocorrelation within each structure.

The results showed that the heating process induced a phase transition from the Amm2 phase to the plastic mesophase for the $[(CH_3)_4N][FeCl_4]$ crystal, while the $[(CH_3)_4N][FeBr_4]$ crystal did not seem to reach the high temperature plastic mesophase. This was likely due to steric hindrance of the $[(CH_3)_4N]$ molecules in the $[(CH_3)_4N][FeBr_4]$ crystal, and that the transition to the mesophase in $[(CH_3)_4N][FeBr_4]$ requires higher temperatures than in $[(CH_3)_4N][FeCl_4]$. These findings agreed well with the analysis of the rotational dynamics of the two crystals, where the results demonstrated that there was more rotational freedom within the $[(CH_3)_4N][FeCl_4]$ crystal than within the $[(CH_3)_4N]$ $[FeBr_4]$ crystal and that the rotational freedom of the molecules increased with increasing temperature.

SAMMENDRAG

Plastiske krystaller er en ny materialklasse med glimrende piezoelektriske og ferroelektriske egenskaper, i tillegg til å være myke og fleksible grunnet rotasjonsfriheten til molekylene. Dette gjør dem til lovende kandidater for å erstatte bly-baserte ferroelektriske materialer i metall-oksid-keramikkbransjen, som et bærekraftig, resirkulerbart og billig alternativ. I tillegg kan plastiske krystaller potensielt brukes i applikasjoner som termisk energilagring og til å forbedre den ioniske ledningsevnen i Li-ionebatterier. Imidlertid er plastiske krystaller dårlig forstått på et mikroskopisk nivå, og de er vanskelige å modellere siden rotasjonsfriheten til molekylene gjør dem svært uordnede.

Målet med denne oppgaven var å forutsi faseovergangene og studere rotasjonsdynamikken i de plastiske krystallene tetrametylammonium-klorotetraferrat ($[(CH_3)_4N][FeCl_4]$) og tetrametylammonium-bromotetraferrat ($[(CH_3)_4N][FeBr_4]$) ved å bruke *ab initio* molekylærdynamikksimuleringer med maskinlærte kraftfelt. Faseovergangene ble studert ved å undersøke endringene i gitter-parametere, enhetscellevolum samt XRD-spektrene til de to forbindelsene ved oppvarming fra 200 K til 400 K og tilbake igjen, og rotasjonsdynamikken ble studert ved å analysere autokorrelasjonen i hver krystall.

Resultatene viste at oppvarmingsprosessen induserte en faseovergang fra Amm2-fasen til den plastiske mesofasen for $[(CH_3)_4N][FeCl_4]$-krystallen, mens $[(CH_3)_4N][FeBr_4]$-krystallen ikke så ut til å nå denne plastiske mesofasen. Dette skyldes antageligvis sterisk hindring av $[(CH_3)_4N]$-molekylene i $[(CH_3)_4N][FeBr_4]$-krystallen, og at overgangen til mesofasen i $[(CH_3)_4N][FeBr_4]$ krever høyere temperaturer enn i $[(CH_3)_4N][FeCl_4]$. Dette stemte bra overens med analysen av rotasjonsdynamikken i de to krystallene, hvor resultatene viste at det var mer rotasjonsfrihet i $[(CH_3)_4N][FeCl_4]$-krystallen enn i $[(CH_3)_4N][FeBr_4]$-krystallen, og at rotasjonsfriheten økte med økende temperatur.

CONTENTS

LIST OF FIGURES

LIST OF TABLES

LISTINGS

ACRONYMS

BEEF	Bayesian error estimate of forces
BZ	Brillouin zone
DFT	density functional theory
GGA	generalized gradient approximation
LDA	local density approximation
MD	molecular dynamics
MLFF	machine learned force fields
PBC	periodic boundary conditions
PBE	Perdew-Burke-Ernzerhof
PBEsol	Perdew-Burke-Ernzerhof revised for solids
SIE	self-interaction error
TEA	tetraethylammonium
TMA	tetramethylammonium
VASP	Vienna *ab initio* Simulation Package
XRD	X-ray diffraction

1 INTRODUCTION

Since the discovery of ferroelectric properties in the Rochelle salt by Valasek in 1920, ferroelectrics have played a vital role in technological advancements, becoming ubiquitous in electronic devices such as sensors, actuators, and capacitors [3–5]. These materials are characterised by their switchable and spontaneous polarisation, in addition to their dielectric and piezoelectric coefficients [4]. This unique set of properties have positioned them as a subject of extensive research, driven by the global interest in ferro- and piezoelectric applications. However, most of the ferroelectric materials dominating this industry today are metal oxide ceramics discovered in the 1940's and 1950's, like barium titanate ($BaTiO_3$, BTO) and lead zirconate titanate ($Pb[Zr_xTi_{1-x}]O_3$, PZT) [5, 6]. Although these materials exhibit exceptional piezoelectric properties [7], the use of environmentally harmful pollutants such as lead needs to be reduced.

Moreover, metal oxide ceramics are in general hard and brittle materials, requiring high processing temperatures in addition to contain dopants such as rare-earth metals in order to improve their flexibility and cover a wider range of functionality [6, 8]. This makes recycling of the materials more difficult, in addition to increasing the elemental footprint, meaning the number of elements from the periodic table added to a compound and their impact in terms of sustainability, recyclability, toxicity, ethics etc [9]. Trying to reduce the elemental footprint and at the same time enhance the functionalities of electronic devices, new and sustainable ferroelectric materials with properties that can match those of BTO and PZT must be developed.

Plastic crystals emerge as a novel class of materials that potentially can meet these requirements. In addition to their excellent ferroelectric and piezoelectric properties, plastic crystals are soft and flexible, and require lower processing temperatures compared to metal oxide ceramics. Plastic crystals are also easier to recycle, consisting of relatively cheap and nontoxic elements [10]. Furthermore, plastic crystals have the ability of absorbing and releasing energy through solid-solid phase transitions, making them promising candidates for thermal energy storage. Another exciting application is for ionic conductors, particularly for Li or Na-ion batteries, due to the flexibility of these materials [11, 12]. Also, an interesting research area for these materials is crystal engineering, where the properties of the crystals can be modified by changing the composition or using variations of the same chemical species, without introducing foreign elements.

Plastic crystals are characterised by possessing a plastic mesophase at a moderate temperature below their melting temperature. The properties of this plastic mesophase are between those of a solid and a liquid, and the molecules gain rotational freedom without breaking the long-range crystallographic order. This makes the material flexible and enables plastic deformations of the crystal, thereby the name plastic crystals.

Although plastic crystals have attracted considerable interest due to their unique properties, the mechanisms behind their behaviour are not yet fully understood on a microscopic level, both from an experimental and from a simulations perspective. These materials are highly disordered and therefore difficult to model, and as a result they have mostly been neglected when it comes to computational modelling. Further research is therefore necessary to gain deeper insights into the rotational dynamics, phase transitions, and functional characteristics of these materials.

1.1 AIM OF THE WORK

In this thesis, two different plastic crystals were investigated; tetramethylammonium irontetrachloride, $[(CH_3)_4N][FeCl_4]$, and tetramethylammonium irontetrabromide, $[(CH_3)_4N][FeBr_4]$. The overall goal was to study and predict the phase transitions and rotational dynamics of these materials through *ab initio* molecular dynamics (MD) simulations with machine learned force fields, to allow for longer length scales than traditional *ab initio* MD whilst retaining the accuracy. The machine learned force fields were trained on-the-fly, which means that they were generated during an *ab initio* MD simulation. The final force fields were then used to simulate phase transitions in the two plastic crystals by heating them from 200 K to 400 K, followed by a cooling process from 400 K to 100 K. This was done using a Langevin thermostat (variable volume) over the course of 1600 ps in total. An analysis of the rotational dynamics was carried out at constant volume, by using the Nosé-Hoover thermostat and calculating the autocorrelation function for the tetramethylammonium molecules at 200 K, 300 K and 400 K.

2 THEORETICAL BACKGROUND

This thesis details the mechanisms behind phase transitions in plastic crystals and the properties of different crystal phases. The aim of this chapter is to give a brief introduction to ferroelectricity and piezoelectricity, phase transitions in plastic crystals as well as an introduction to the compounds TMA[$FeCl_4$] and TMA[$FeBr_4$] studied in this project.

2.1 FERROELECTRICITY AND PIEZOELECTRICITY

Traditionally, solids have been divided into three different material classes based on their electrical properties. Metals conducts electricity well, semiconductors conducts poorly and insulators don't conduct electricity at all. Insulators are often referred to as dielectrics, and are characterised by their dielectric constant, or relative permittivity ϵ_r. When an external electric field is applied to a dielectric material, the electrons in the material are displaced slightly from their positions, but they do not move freely through the material like in a metal. The external field will make the electron cloud asymmetrically distributed around the positively charged nucleus, turning each atom into a small dipole. This results in a polarisation of the material. The relative permittivity ϵ_r is a measure of how easy the material can become polarised in an electric field [13].

In some dielectric materials, there is an additional relationship between the mechanical and the electrical state of the material. This behaviour is termed piezoelectricity. As figure 2.1a illustrates, the electrical charge in the material will be evenly distributed in an unstressed state. However, when the solid is subjected to a mechanical stress such as pressure, it becomes polarised, generating an electrical potential. This is termed the direct piezoelectric effect. When a stress σ_j induces a polarisation P_i in the material under a constant electric field E, the piezoelectric coefficients $d_{i,j}$ can be described mathematically by $d_{i,j} = (dP_i/d\sigma_j)^E$. Piezoelectric materials also have the converse effect, where an electrical field E_j can be used to induce a mechanical strain ϵ_i in the material, $d_{i,j} = (d\epsilon_i/dE_j)^\sigma$ [14]. In other words, an electric field can be used to make the material contract or expand in a certain direction. This effect is utilised in e.g. quartz oscillators [13].

Pyroelectric materials are a subset of piezoelectric materials. They have the properties of piezoelectrics, but in addition they have a spontaneous, temperature dependent polarisation $\mathbf{P}_s$ even when no elec-

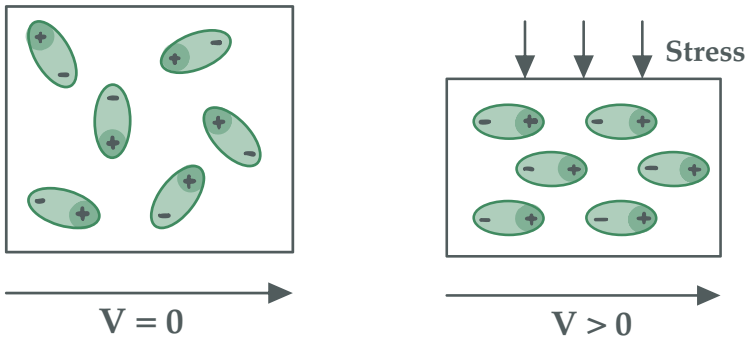

(a) Unstressed state. (b) Stressed state.

Figure 2.1: Piezoelectric material (a) without and (b) with an applied mechanical stress. The stress induces a polarisation in the material, generating a voltage.

tric field or mechanical stress is applied. This polarisation changes when the material is subjected to a temperature change.

In some pyroelectrics, the natural, spontaneous polarisation $\mathbf{P}_s$ can be switched when the material is exposed to an electric field. This effect is known as ferroelectricity. Reversing the polarisation of the material by changing the electric field yields a hysteresis loop, and the polarisation of a ferroelectric material will therefore be history dependent [4]. The relationship between piezoelectricity, pyroelectricity and ferroelectricity is illustrated in figure 2.2.

2.1.1 *Crystal symmetry and ferroelectric properties*

Crystal symmetry plays an important role when it comes to the piezoelectric and ferroelectric properties of the system. There are seven crystal systems (triclinic, monoclinic, orthorhombic, tetragonal, trigonal, hexagonal, and cubic), and these can be divided into 32 crystal classes, or point groups, representing the 32 unique ways of combining symmetry elements in a crystal [13].

In a crystal where the unit cell has a center of symmetry, the overall polarisation will always be zero because any distortion of ions causing a dipole will be canceled out by another dipole pointing in opposite direction somewhere else in the crystal. Therefore, piezoelectricity can only arise in the 21 non-centrosymmetric point groups. All but one of these 21 groups display electric polarisation when exposed to external stress, giving 20 piezoelectric point groups (see figure 2.2). In order to produce a spontaneous polarisation when no external field is present, a unique polar axis is required. Of the 20 piezoelectric groups, 10 of them fulfil this criterion, giving 10 pyroelectric classes. These can further be divided into ferroelectric and non-ferroelectric ones, as illustrated in figure 2.2.

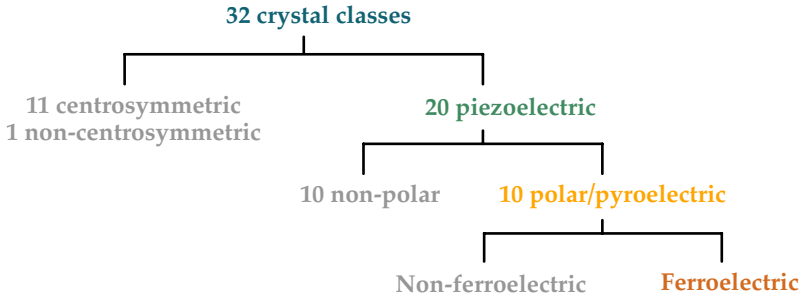

Figure 2.2: Schematic showing the relation between piezoelectrics, pyroelectrics and ferroelectrics. Figure inspired by [13].

2.2 PHASE TRANSITIONS

Phase transitions are the physical processes by which a material undergoes a change in its physical state or structure, such as changing from a solid to a liquid. In ferroelectric materials, the spontaneous polarisation $\mathbf{P}_s$ normally decreases with temperature and vanishes completely at a critical temperature called the Curie temperature, T_C. By heating the material above T_C, a phase transition from a ferroelectric to a paraelectric phase will take place. Paraelectric materials are a subgroup of dielectrics that do not have a permanent electric dipole moment like pyroelectrics and ferroelectrics.

The ferroelectric to paraelectric transition at T_C is an example of a solid-solid phase transition. Solid-solid phase transitions are transitions where the crystal structure changes while the material remains in the solid state. As different crystal structures possess different electrical properties, a phase transition may involve a change in the dielectric, piezoelectric or ferroelectric properties of a crystal. The transition from the ferroelectric phase to the paraelectric phase is normally characterised as a displacive phase transition. This means that the high temperature phase far above T_C is highly ordered and centrosymmetric, but by cooling the material down below T_C the cations are collectively displaced from their mean positions, resulting in the ferroelectric state. However, the ferroelectric phase transition could also be described as an order-disorder transition, which is often the case for ferroelectric plastic crystals. In order-disorder transitions the degree of molecular ordering within the crystal lattice changes during the phase transition. Well above T_C the ions are in a disordered state, and as the temperature decreases towards T_C the local ordering of cations starts to increase. Below T_C the displacements of the ions are perfectly ordered in the ferroelectric state.

2.3 PLASTIC CRYSTALS

Plastic crystals are materials that exhibit a cubic mesophase with properties in between those of a liquid and a solid. Examples include quinuclidinium perrhenate ($HQRO_4$), adamantane ($C_{10}H_{16}$), succinonitrile ($C_2H_4(CN)_2$) and tetrabromomethane (CBr_4) [10, 12, 14–17]. Plastic crystals were first recognised and named by Timmermanns in 1935 [18].

In the solid crystalline phase, the molecules are arranged in a periodic lattice with long-range crystallographic order. Each lattice point have vibrational freedom, but the molecules are fixed at their lattice positions. By increasing the temperature, a transition to the plastic mesophase will find place. Here, the molecules gain rotational freedom, as illustrated in figure 2.3. The rotation of the molecules around their mass centre creates a local disorder, without breaking the long-range crystallographic order. By further increasing the temperature, a transition to the liquid phase will take place. In the liquid phase, molecules have translational freedom in addition to vibrational and rotational freedom, allowing them to move around freely. Figure 2.3 illustrates the difference between these three phases, and a summary of the degrees of freedom for each phase can be found in table 2.1.

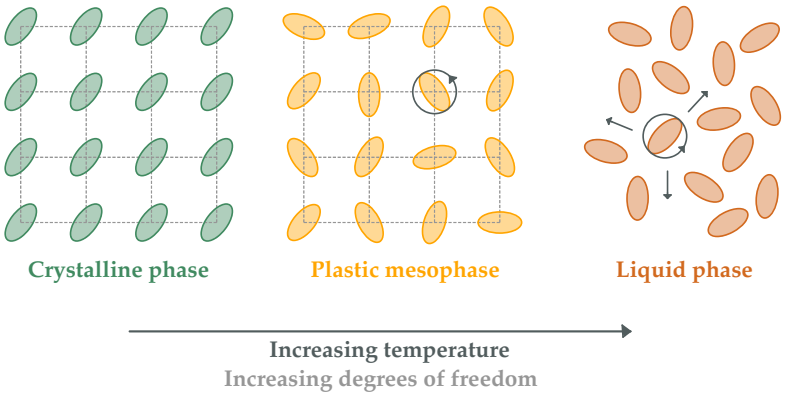

Figure 2.3: Schematic showing the relation between the solid crystalline phase, the plastic mesophase and the liquid phase. The molecules in the solid phase only have vibrational freedom, while the molecules in the plastic mesophase also have rotational freedom. In the liquid phase, molecules gain translational freedom as well, indicated by the grey arrows. Figure retrieved from [2].

Plastic crystals are characterised by having low entropies of melting and relatively high melting points. This can be seen in connection with the rotational freedom in the plastic mesophase, as this rotational disorder makes the energy barrier of going from the plastic mesophase to the liquid phase lower compared to the energy barrier of going directly from the crystalline phase to the liquid phase in non-plastic crystals. Macroscopically, the transition from the crystalline

Table 2.1: Degrees of freedom for the molecules in a crystalline, plastic and liquid phase.

PHASE	VIBRATION	ROTATION	TRANSLATION
Crystalline phase	X	-	-
Plastic mesophase	X	X	-
Liquid phase	X	X	X

phase to the plastic mesophase in plastic crystals can be observed in the high entropies following this transition. When the molecules already have gained rotational freedom, the transition to the liquid state is associated with a smaller change in entropy. In contrast, non-plastic crystals exhibit a larger disparity between their solid and liquid states, resulting in higher entropies of melting.

Plastic crystals normally consist of globular molecules. The rotation of the molecules makes the effective volume occupied by each molecule approximately spherical, allowing a dense cubic packing structure with many available slip planes. The lattice spacing will also be larger in a plastic crystal compared to a crystalline solid due to the rotation of the molecules, resulting in weaker interactions between each lattice point. This in combination with the many possible slip systems results in plastic deformations, which is the reason why these materials are called plastic crystals.

2.3.1 *TMAFeCl4 and TMAFeBr4*

There are many different types of plastic crystals, e.g. quinuclidinium perrhenate ($HQReO_4$), which is a ferroelectric plastic crystal suitable for energy harvesting applications [10, 14], and succinonitrile, which is a promising candidate to improve the performance of Li-ion batteries [19].

This project involved the investigation of two different plastic crystals: tetramethylammonium irontetrachloride ($[(CH_3)_4N][FeCl_4]$) and tetramethylammonium irontetrabromide ($[(CH_3)_4N][FeBr_4]$). They have the organic globular tetramethylammonium [tetramethylammonium (TMA)]$^+$ cation in common, which consists of one nitrogen atom surrounded by four methyl groups as illustrated in the schematic below. The inorganic anions $[FeCl_4]^-$ and $[FeBr_4]^-$ have the same tetragonal structure, with one iron atom surrounded by four chlorine or bromine atoms. The halogen element differs in order to examine of dissimilarities between chlorine and bromine.

Previous experiments have shown that the rotational disorder in these plastic crystals mainly is due to the rotational freedom of the TMA molecules, and the positions of the inorganic anions are rela-

tively well defined. However, both the organic cations and the inorganic anions play an important role when it comes to determining the properties of the compounds, and previous work have shown that the choice of halogen element (Cl or Br) affects both the lattice parameters and the electronic properties of these crystals [2].

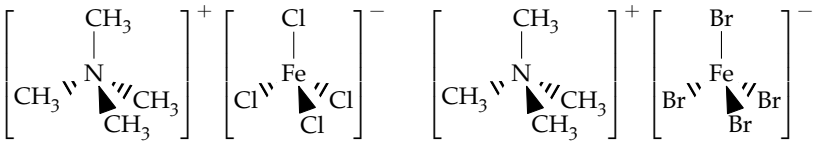

$TMA[FeCl_4]$ $TMA[FeBr_4]$

Upon heating or cooling, there have been reported four different solid-solid phase transitions for these plastic crystals, giving a total of five different crystal structures as illustrated in figure 2.4. The different structures are labeled from I to V, where phase I is stable at the highest temperature and phase V is stable at the lowest temperature. Phase I ($Pm\bar{3}m$) is cubic and paraelectric, and stable at temperatures above 400 K. By lowering the temperature, a transition to phase II (Cmcm) will take place. Phase II is stable at around 360 K, and is orthorhombic and paraelectric. By further lowering the temperature, phase III (Amm2) and IV (Pma2) will appear at 330 K and 300 K, respectively. Both III and IV are ferroelectric structures. Finally, by lowering the temperature to about 250 K, a transition to phase V (Pbcm) will find place. Phase V is orthorhombic and paraelectric. These crystal data are retrieved from a study of the plastic crystal $TMA[FeCl_4]$ by Harada *et al* in 2018 [20], and are summarised in table 2.2.

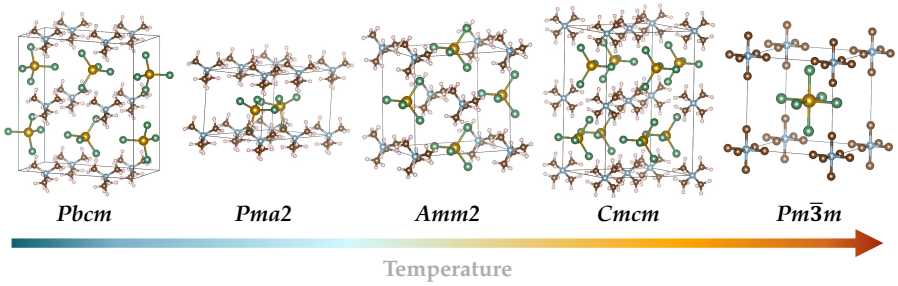

Figure 2.4: Visual presentation of the five space groups of the $TMA[FeCl_4]$ crystal. From left to right, the crystals are organised from the lowest temperature phase to the highest temperature phase.

Plastic crystals are difficult to model due to the rotational freedom of the molecules. The plastic mesophase is highly disordered as this is the final intermediate state before the crystal melts to the liquid phase, and although this mesophase have been assigned the cubic $Pm\bar{3}m$ space group, it is important to keep in mind that there is a lot of movement in the crystal structure at this point. Defining lattice

Table 2.2: Overview of the five different space groups of the TMA[$FeCl_4$] crystal. Crystal data retrieved from [20].

PHASE	TEMPERATURE [K]	CRYSTAL SYSTEM	SPACE GROUP
I	400	cubic	$Pm\bar{3}m$
II	360	orthorhombic	Cmcm
III	330	orthorhombic	Amm2
IV	300	orthorhombic	Pma2
V	250	orthorhombic	Pbcm

parameters and other crystal properties for this plastic mesophase is therefore not straightforward, as most of the symmetry is broken at this point due to the rotational disorder.

3 DENSITY FUNCTIONAL THEORY

Understanding the mechanisms underlying the molecular rotations in plastic crystals is challenging through experimental studies due to the vast number of potential crystal configurations resulting from the rotational freedom of the molecules. Consequently, simulation-based methods, such as density functional theory (DFT), are commonly employed as an approach to investigate these materials.

Density functional theory (DFT) is a powerful modelling method utilizing quantum mechanical laws and principles. The calculations are performed at the absolute zero temperature 0 K limit, with the objective of determining the ground state electron density of many-body systems. The ground state electron density can then be used to calculate other material properties.

The purpose of this chapter is to give a brief introduction to DFT. The equations and theoretical background in sections 3.1 - 3.6 are primarly based on [21]. This chapter also includes a brief introduction to the Vienna *ab initio* Simulation Package (VASP)[1] package, a powerful tool extensively used for DFT simulations.

3.1 QUANTUM MECHANICAL BACKGROUND

The quantum mechanical state of a system can be described by the wave function ψ, which can be found by solving the Schrödinger equation, $H\psi = E\psi$. Here, H is the Hamiltonian operator and E is the set of energies (eigenvalues) that corresponds to the solutions (ψ, eigenfunctions) of the equation. Although the Schrödinger equation can be solved analytically for a few simple systems, the equation becomes more complex for many-body systems like the plastic crystals studied in this project. In the case of crystalline solids, the interactions between nuclei and electrons, between each individual electron and all other electrons, as well as the interactions between each individual nucleus and all other nuclei must be considered. Solving the Schrödinger equation exactly is therefore almost impossible in most cases, and various simplifications have been introduced in order to approximate the wave function ψ. One of these is the Born-Oppenheimer approximation, which involves a separation of the nuclei and electrons into different mathematical problems. Since the nucleus is much heavier than the electrons, the nucleus appear fixed from the electrons perspective, while the electrons seem to update their position instantly from the nucleus' perspective. The motion of

1 *ab initio* means that the method is based on first principles.

the electrons can therefore be assumed to be independent of the motion of the nuclei. Ignoring the kinetic energy contribution from the nuclei, the Schrödinger equation reduces to

$$\left[-\frac{\hbar^2}{2m}\sum_{i=1}^{N}\nabla_i^2+\sum_{i=1}^{N}V(\mathbf{r}_i)+\sum_{i=1}^{N}\sum_{j<i}U(\mathbf{r}_i\mathbf{r}_j)\right]\psi=E\psi, \tag{3.1}$$

where m is the electron mass and ψ is the total electron wave function. From left to right, the three terms in the brackets represents the kinetic energy of each electron, the Coulomb interactions between the electrons and the nuclei and the Coulomb interactions between pairs of electrons.

The electron wave function ψ is a function of the three spatial coordinates for each of the N electrons in the system, $\psi=\psi(\mathbf{r}_1,\dots,\mathbf{r}_N)$. This expression can be approximated to a product of the N individual wave functions, $\psi=\psi(\mathbf{r}_1)\psi(\mathbf{r}_2)\dots\psi(\mathbf{r}_N)$, known as the Hartree product. This equation has $3N$ dimensions, which means that even for simple systems like the CO_2 molecule, the wave equation will have 66 dimensions (3 dimensions for each of the 22 electrons) [21]. Solving the Schrödinger equation explicitly for larger systems would therefore be an expensive procedure.

3.2 THE HOHENBERG-KOHN THEOREMS

Density functional theory (DFT) is a solution to this many-body-problem, and rests on two fundamental theorems proved by Hohenberg and Kohn, in addition to a set of equations derived by Kohn and Sham. The first Hohenberg-Kohn theorem states that

> *The ground-state energy from Schrödinger's equation is a unique functional of the electron density.* ([21])

The ground state energy can therefore be expressed as $E=E[n(\mathbf{r})]$, where the electron density $n(\mathbf{r})$ is related to the individual electron wave functions through

$$n(\mathbf{r})=2\sum_i\psi_i^*(\mathbf{r})\psi_i(\mathbf{r}). \tag{3.2}$$

The factor of 2 is to count for spin, since each individual wave function can be occupied by two electrons if they have opposite spins according to the Pauli exclusion principle. This theorem implies that by determining the ground state electron density, one can find the ground state energy and therefore solve the Scrödinger equation, simplifying the problem from $3N$ dimensions to only 3 spatial dimensions.

The second Hohenberg-Kohn theorem states that

> *The electron density that minimizes the energy of the overall functional is the true electron density corresponding to the full solution of the Schrödinger equation.* ([21])

In other words, if the true functional was known, one could have determined the ground state electron density by varying $n(\mathbf{r})$ and found the one that minimised $E[n(\mathbf{r})]$. Unfortunately, the energy functional is unknown and needs to be approximated.

3.3 THE KOHN-SHAM EQUATIONS

From equation 3.2, it is clear that the total electron density is defined by the individual electron wave functions $\{\psi_i\}$. The energy functional can therefore be written in terms of these,

$$E[\{\psi_i\}] = E_{known}[\{\psi_i\}] + E_{XC}[\{\psi_i\}], \tag{3.3}$$

where the energy functional have been split into known and unknown terms. $E_{known}[\{\psi_i\}]$ consists of a kinetic energy term, an electron-nuclei attraction term and an electron-electron repulsion term. The unknown part $E_{XC}[\{\psi_i\}]$ is called the exchange-correlation functional, and includes all quantum mechanical effects not included in the known terms.

Kohn and Sham showed that the task of determining the electron density could be split into a set of single electron Schrödinger equations, where each equation only involved a single electron. These are called the Kohn-Sham equations, and have the form

$$\left[-\frac{\hbar^2}{2m}\nabla^2 + V(\mathbf{r}) + V_H(\mathbf{r}) + V_{XC}(\mathbf{r})\right]\psi_i(\mathbf{r}) = \epsilon_i\psi_i(\mathbf{r}). \tag{3.4}$$

From left to right, the first term in the brackets represents the kinetic energy of the electron and the second term represents the attractive interaction between the electron and the collection of atomic nuclei. The third term ($V_H(\mathbf{r})$) is called the Hartree potential and represents the repulsive interaction between the electron and the overall electron density, and the fourth term ($V_{XC}(\mathbf{r})$) is the exchange-correlation functional. Since each electron in the system also contributes to the overall electron density, the Hartree potential involves an unphysical interaction between each electron in the system and itself. This is called the self-interaction error (SIE), and the correction for this is included in the exchange-correlation functional. The Hartree potential is defined by

$$V_H(\mathbf{r}) = e^2\int \frac{n(\mathbf{r}')}{|\,\mathbf{r}-\mathbf{r}'\,|}d^3r'. \tag{3.5}$$

The exchange correlation functional can be described by a functional derivative of the exchange-correlation energy $E_{XC}(\mathbf{r})$,

$$V_{XC}(\mathbf{r}) = \frac{\delta E_{XC}(\mathbf{r})}{\delta n(\mathbf{r})}, \tag{3.6}$$

where δ have been used instead of d to emphasize that this is a functional derivative.

3.4 THE IONIC AND ELECTRONIC LOOP

From equation 3.4, it is clear that in order to solve the Kohn-Sham equations, the Hartree potential must be known. However, in order to calculate the Hartree potential, one must first determine the electron density (equation 3.5), and to calculate the electron density one must know all the individual electron wave functions (equation 3.2). These, in turn, can be found by solving the Kohn-Sham equations. To break this circle of dependencies, the problem is normally treated in an iterative way as shown below.

1. Guess an initial electron density $n(\mathbf{r})$.
2. Solve the Kohn-Sham equations by using the trial electron density to find the individual electron wave functions, ψ_i.
3. Use equation 3.2 to calculate a new electron density, $n_{new}(\mathbf{r})$.
4. Compare $n_{new}(\mathbf{r})$ with the initial electron density. If they are equal[2], this is the ground state electron density. Otherwise, update the trial electron density and continue from step 2.

This is called the electronic loop. When the loop has converged, the final electron density is used to calculate the forces on all the atomic nuclei, and the nuclei are then moved according to the calculated forces. With the new ionic configuration, the electronic structure is then relaxed again, followed by a new adjustment of the ionic positions. This process continues until both the inner electronic loop and the outer ionic loop has converged.

3.5 THE EXCHANGE-CORRELATION FUNCTIONAL

Although the calculation scheme presented above may appear relatively simple, a critical complication factor is that the true exchange-correlation functional is not known. To solve the Kohn-Sham equations, $V_{XC}(\mathbf{r})$ therefore needs to be approximated.

2 A convergence criterion is used to determine how close the two electron densities needs to be before they are considered to be the same.

One of the simplest approximations is the local density approximation (LDA), that utilizes the fact that the exchange-correlation functional of a uniform electron gas is known. In this case, the electron density $n(\mathbf{r})$ is constant, and it is assumed that for every position $\mathbf{r}$ the exchange-correlation potential equals the known exchange-correlation potential for the uniform electron gas at the local electron density $n(\mathbf{r})$ observed at that position,

$$V_{XC}(\mathbf{r}) = V_{XC}^{\text{electron gas}}(\mathbf{r})[n(\mathbf{r})]. \tag{3.7}$$

Another common approximation to the exchange-correlation functional is the generalized gradient approximation (GGA), using both the local electron density and the local gradient in the electron density to calculate $V_{XC}(\mathbf{r})$. The local gradient can be included in the calculation in several different ways, resulting in a large number of different GGA functionals. Two of the most common ones are the Perdew-Burke-Ernzerhof (PBE) functional and the Perdew-Burke-Ernzerhof revised for solids (PBEsol) functional. In this project, the PBEsol functional was used in all the DFT calculations.

3.5.1 *The Hubbard 'U' Parameter*

As mentioned above, the Hartree potential involves a self-interaction error (SIE) between each electron in the system and itself. The Hubbard 'U' parameter is a correction for this error, corresponding to the difference between the ionisation energy (I) and the electron affinity (A) of an atom, $U = I - A$ [13]. To get a better understanding of this, suppose we have two isolated atoms in the ground state with only a single valence electron each. The ionisation energy refers to the amount of energy required to remove the valence electron from one of the atoms, while the electron affinity is the energy gained by giving the electron to the other atom. The Hubbard 'U' factor can therefore be interpreted as the extra energy due to electron-electron repulsion between the two electrons now being on the same atomic core.

The Hubbard 'U' correction describes strongly correlated electrons in the d and f orbitals, and results in a better localisation of these electronic states. Without the U parameter, the LDA and GGA functionals tends to delocalise the d and f electrons resulting in an underestimation of the electronic band gap. As a consequence, DFT sometimes predicts metallic behaviour for semiconducting materials. To get a better description of the electronic and magnetic properties of materials it is therefore important to include the Hubbard 'U' factor.

3.6 COMPUTATIONAL APPROACHES TO DFT

To reduce the computational load of a DFT calculation, there are several simplifications to make the task of solving the Schrödinger equation less exhausting.

3.6.1 *Energy cutoff*

In a periodic potential, the single electron solutions (eigenfunctions) of equation 3.4 may be expressed as a product of a periodic function and a plane wave,

$$\phi_{\mathbf{k}}(\mathbf{r}) = \exp(i\mathbf{k}\cdot\mathbf{r})u_k(\mathbf{r}), \tag{3.8}$$

where $u_k(\mathbf{r})$ has the same periodicity as the supercell. This is known as Bloch's theorem. The periodic function $u_k(\mathbf{r})$ can further be expanded as a Taylor series,

$$u_k(\mathbf{r}) = \sum_{\mathbf{G}} c_{\mathbf{G}} \exp\left[i\mathbf{G}\cdot\mathbf{r}\right], \tag{3.9}$$

which is a sum over reciprocal lattice vectors $\mathbf{G} = m_1\mathbf{b}_1 + m_2\mathbf{b}_2 + m_3\mathbf{b}_3$ where m_i are integers. From the definition of reciprocal lattice vectors, this means that for any real lattice vector $\mathbf{a}_i$, $\mathbf{b}_j \cdot \mathbf{a}_i = 2\pi\delta_{ij}$ and $\mathbf{G}\cdot\mathbf{a}_i = 2\pi m_i$ [21]. Combining equation 3.8 and 3.9 therefore yields

$$\phi_{\mathbf{k}}(\mathbf{r}) = \sum_{\mathbf{G}} c_{\mathbf{k}+\mathbf{G}} \exp\left[i(\mathbf{k}+\mathbf{G})\mathbf{r}\right]. \tag{3.10}$$

This means that in order to solve the Schrödinger equation for even a single point in $\mathbf{k}$-space, a summation over infinitely many $\mathbf{G}$-vectors is required. This is not feasible in a numerical perspective, so in order to reduce the number of summations, the energy of the plane wave with wavevector $\mathbf{k}' = \mathbf{k} + \mathbf{G}$ is considered

$$E = \frac{\hbar^2}{2m} |\, \mathbf{k} + \mathbf{G} \,|^2 \tag{3.11}$$

Because the system tends to minimise its energy, it is reasonable to assume that the low energy solutions are more physical significant than the high energy solutions. Therefore, the infinite sum is truncated to only include reciprocal lattice vectors up to a certain $\mathbf{G}_{\text{cut}}$,

$$\phi_{\mathbf{k}}(\mathbf{r}) = \sum_{|\mathbf{G}+\mathbf{k}|<G_{\text{cut}}} c_{\mathbf{k}+\mathbf{G}} \exp\left[i(\mathbf{k}+\mathbf{G})\mathbf{r}\right], \tag{3.12}$$

which gives an energy cutoff of

$$E_{cut} = \frac{\hbar^2}{2m} {G_{cut}}^2. \tag{3.13}$$

In this project, the cutoff energy was determined by investigating the convergence of the total energy with respect to different values of E_{cut}.

3.6.2 *K-point density*

A consequence of Bloch's theorem is that all unique reciprocal lattice vectors **k** can be found within the 1st Brillouin zone (BZ). Since any vector outside this zone can be translated back into the 1st BZ by applying another appropriate reciprocal lattice vector, going outside the 1st BZ doesn't provide any new physical information about the system. This reduces the problem to only solving the Schrödinger equation within the 1st BZ. However, there are infinitely many **k**-vectors within this zone, and the 1st BZ must therefore be discretised into a **k**-point grid in order to solve the wave equation numerically. The more **k**-points included, the higher accuracy of the calculation, but more **k**-points also increases the computational demand. To find the optimal **k**-point density, the convergence of the total energy with respect to the **k**-point density can be investigated.

3.6.3 *Pseudopotentials*

Since shorter lattice vectors in real space corresponds to larger lattice vectors in resiprocal space, a large energy cutoff must be used to include the plane waves oscillating on a short scale in real space. This is the case for the tightly bound core electrons, however the core electrons are usually not considered important from a physical point of view. The physical properties of the material are more dependent of the valence electrons. Therefore, pseudopotentials can be used to replace the electron density of the core electrons with a fixed, smoothed density chosen to match the real properties of the atomic core. With this frozen core approximation only the electrons in the outer shells are free to move and needs to be calculated, which drastically reduces the computational load. Pseudopotentials with low cutoff energies are normally referred to as soft, while pseudopotentials requiring high cutoff energies are hard. Typically, DFT codes provide a library of pseudopotentials for each element in the periodic table.

3.7 THE VIENNA AB INITIO SIMULATION PACKAGE

The Vienna *ab initio* Simulation Package (VASP) [22–24] is a powerful computer program used for DFT calculations. Descriptions of the

main input and output files used in a VASP calculation are presented below.

3.7.1 *Input files*

The four most important input files, required in any VASP calculation, are the `INCAR` file, the `KPOINTS` file, the `POSCAR` file and the `POTCAR` file.

The **`INCAR`** file is the primary input file, and contains a list of various parameters controlling the calculation. These settings are given on the format *`TAG = value`*, and specify e.g. which algorithm to use, convergence criteria, temperature, the number of ionic steps etc. Some of the most important tags used in this project are presented in listing 3.1.

Listing 3.1: A short description of the most important INCAR parameters.

```
ENMAX            % Plane-wave energy cutoff
EDIFF            % Convergence criterion, electronic loop
EDIFFG           % Convergence criterion, ionic loop
NSW              % Maximum number of ionic steps
ISIF             % Stress/relaxation
NBLOCK           % Update XDATCAR every n steps
POTIM            % Timestep in fs
MDALGO           % MD algorithm; 2=Nose-Hoover; 3=Langevin
LANGEVIN_GAMMA   % Friction
LANGEVIN_GAMMA_L % Lattice friction
PMASS            % Lattice mass
TEBEG            % Start temperature
TEEND            % End temperature
ML_ISTART        % Operation mode of MLFF method
```

The **`KPOINTS`** file defines the **k**-point grid used to map the 1st Brillouin zone. For cubic systems, the **k**-points are typically evenly distributed in the x, y, and z directions, and if M **k**-points are used in each direction, it is referred to as an M×M×M **k**-grid.

The **`POSCAR`** file contains information about the lattice geometry and all the ionic positions. This file can also be used to give the starting velocities of the atoms.

The **`POTCAR`** file contains all the pseudopotentials for the different atomic species used in the calculation.

3.7.2 *Output files*

Depending on the type of calculation, there are many possible output files from a VASP calculation. Hereunder is given a brief explanation of some of the most important ones for this project.

The **OUTCAR** file is the main output file, and contains information about e.g. the electronic steps, stress tensors, forces on the atoms as well as a summary of the chosen INCAR parameters.

The **CONTCAR** file contains the final ionic positions, written on the same format as the POSCAR file. Hence, the CONTCAR can be used to continue a calculation by copying it over to the POSCAR.

The **XDATCAR** file contains information about each n'th ionic configuration, where n is the number specified by the NBLOCK tag in the INCAR.

The **OSZICAR** file gives a summary of the results from the calculation, e.g. the free energies, temperatures and convergence of the total energy.

4 MOLECULAR DYNAMICS

Molecular dynamics is a computational technique used to study the behaviour of atoms and molecules over time. The transitions from one microstate[1] to another and the particular trajectories of each atom are inconsequential, but the overall statistical distribution can be used to calculate the macroscopic properties of the material. The aim of this chapter is to give a brief introduction to classical molecular dynamics, as well as a introduction to *ab initio* molecular dynamics and the difference between these methods. The theory and equations presented in section 4.1 are mainly based on [25].

4.1 CLASSICAL MOLECULAR DYNAMICS

In classical molecular dynamics (MD), each atom is approximated as a hard sphere obeying the laws of classical mechanics, and the electronic structure is not taken into account. This means that the interatomic potentials are generated from empirical observations and experimental data, since the presence of electrons (being the origin of interatomic potential) is neglected. A classical MD simulation generally proceeds as:

1. Input parameters specifying conditions like temperature, number of particles etc. are read in.
2. Initialisation of the system.
3. Calculation of the forces acting on all particles, given the initial positions, velocities and the interatomic potential.
4. Newton's equations of motion are numerically integrated, and the positions and velocities of the particles are updated.
5. Step 3 and 4 are repeated until the system have reached equilibrium and the system properties does no longer change with time.

Typical system properties of interest could be energies, mechanical properties, thermal expansion coefficient, heat capacity, thermal conductivity, radial distribution function etc.

1 For each macroscopic thermodynamic state, the number of microstates is the number of possible configurations of the system on a microscopic level.

4.1.1 *Initialisation*

Before a MD simulation is started, the system needs to be initialized. This is done by specifying several input parameters such as the number of atoms, their initial positions and velocities, the time step Δt, the total simulation time and the type of ensemble. The number of atoms N should be kept as small as possible to save computational time, but not too small because that would result in unreliable data. Normally, at least 100 atoms are required in order to represent a real system properly. The initial positions are normally specified according to known lattice positions, and the initial velocities could either be zero or chosen from e.g. a Maxwell-Boltzmann distribution. When it comes to the timestep Δt, there is also a trade-off between accuracy and computational time. Normally, smaller time steps improves the accuracy, but increases the computational load of the simulation. A rule of thumb is that atoms should not travel longer than $1/30$ of the nearest neighbour distance during a time step Δt. The total simulation time should be longer than the relaxation time of the system, but not be too long as this may cause error accumulation. Finally, the type of ensemble needs to be chosen. Normally, the microcanonical ensemble (NVE) is chosen for MD simulations, where the system is assumed to be isolated and the number of atoms (N), volume (V) and total energy (E) are kept constant. Other alternatives are e.g. the canonical ensemble (NVT), where N, V and temperature (T) are kept constant, or the isobaric-isothermal ensemble (NpT), where N, pressure (p) and T are kept constant.

4.1.2 *Potentials*

When two atoms are close to each other, there is a balance between the attractive Van der Waals forces due to dipole-dipole interaction and repulsive Pauli forces due to overlapping electron orbitals. The system will always try to minimise its potential energy, so the equilibrium distance between the two atoms corresponds to the bottom of the potential curve, where the attractive and repulsive forces cancel each other out.

From Newton's equations, the sum of forces acting on each atom, $\mathbf{F}$, can be expressed as

$$\mathbf{F} = m\mathbf{a} = m\frac{d\mathbf{v}}{dt} = m\frac{d^2\mathbf{r}}{dt^2} = \frac{d\mathbf{p}}{dt}, \tag{4.1}$$

where m, $\mathbf{a}$, $\mathbf{v}$, $\mathbf{r}$ and $\mathbf{p}$ are the mass, acceleration, velocity, position and momentum of the atom, respectively, and t is time. Normally, the system in MD simulations is isolated, which means that the total energy is constant in time ($dE/dt = 0$). The total force can then be expressed as the negative gradient of the potential with respect

to position, $\mathbf{F} = -\nabla U$. If the potential U is known as a function of distance, the forces on the atoms can be calculated, and the time evolution of the system can be found by using equation 4.1.

The calculation of the forces on all particles is usually the most time consuming step in a MD calculation. By considering all pair-wise interactions in a system of N atoms, it results in $N(N-1)/2 \propto N^2$ pair distances. However, there are several simplifications that can be made to make the computing time scale as N instead of N^2.

Molecular dynamics uses periodic boundary conditions, meaning that the simulation cell is surrounded by an infinite number of mirror images in the x-, y- and z-directions, as shown in figure 4.1. This is done to avoid surface effects and to approximate the behaviour of bulk materials. The actual simulation is only performed on the primary box, but if an atom k in the primary box moves out of the box, one of it's mirror atoms will reappear at the opposite side of the box with the same velocity.

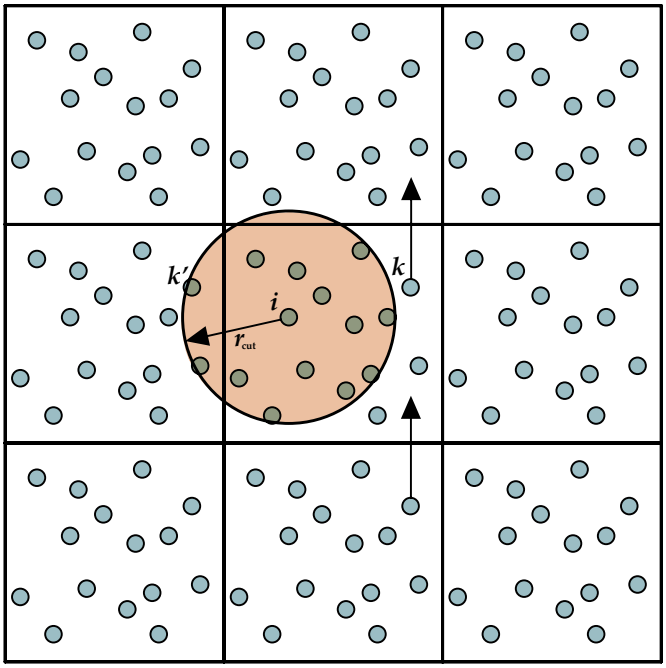

Figure 4.1: Schematic illustrating periodic boundary conditions, where the primary simulation cell is surrounded by mirror images of itself in all three directions. When atom k moves out of the cell, one of its mirror images reappears at the opposite side of the cell. The sphere around atom i illustrates the cutoff radius r_{cut}, where the force between atom i and atom k will be calculated by considering its mirror image k' instead of k, as the distance between i and k is larger than r_{cut}, but the distance between i and k' is shorter than r_{cut}. Figure inspired by [25].

One of the techniques that can be utilized in order to reduce the computational load of MD simulation, is to use a cutoff radius r_{cut} in the calculation of the interatomic potentials. At large distances,

the potential normally tails off and becomes negligible, which means that the interactions between atoms separated by a larger distance than r_{cut} can be disregarded. In order to avoid that one atom in the primary box interacts with both another atom in the primary box and one of its mirror images in the neighbouring boxes, the cutoff radius must me smaller than half of the primary box size. As illustrated in figure 4.1, atom i has a neighbouring atom k in the primary box, but the distance between i and k is larger than the distance between i and the mirror atom k' in the box to the left, so only the interaction between i and k' will be considered in the force calculation. This is called the minimum image convention, and means that each atom in the system interacts with the closest image of its neighbouring atoms.

4.1.3 *Solutions to Newton's equations*

In a system of N atoms, the total force can be expressed as

$$F(\mathbf{r}_1, \mathbf{r}_2, ..., \mathbf{r}_N) = \sum_i m_i \mathbf{a}_i = \sum_i m_i \frac{d^2\mathbf{r}_i}{dt^2}. \tag{4.2}$$

Since the total energy is conserved ($dE/dt = 0$), the negative derivative of the potential energy can be used to obtain the force on atom i,

$$\mathbf{F}_i = m_i \frac{d^2\mathbf{r}_i}{dt^2} = -\frac{dU(\mathbf{r}_i)}{d\mathbf{r}_i}. \tag{4.3}$$

In MD simulations, this ordinary differential equation is solved trough a numerical finite-difference scheme, where the differentials ($d\mathbf{r} \equiv d^3r$ and dt) are replaced by finite differences, Δr and Δt. By doing a Taylor expansion, the position at a time $t + \Delta t$ can then be projected from the position at time t,

$$\mathbf{r}(t + \Delta t) = \mathbf{r}(t) + \mathbf{v}(t)\Delta t + \frac{1}{2!}\mathbf{a}(t)\Delta t^2 + \frac{d^3\mathbf{r}(t)}{3!dt^3}\Delta t^3 + ... \tag{4.4}$$

where the velocity, acceleration and force on each atom are assumed to remain constant during the small discretized time step Δt. Normally, only terms up to third order are considered in a MD simulation, but the accuracy of the calculation can be improved by including higher order terms as well.

The numerical integration of Newton's equations normally proceeds as follows:

1. Given the interatomic potential, the forces acting on all atoms are calculated by using equation 4.3.

2. The corresponding accelerations are calculated by using $\mathbf{a}_i = \mathbf{F}_i/m$.

3. The positions, velocities and accelerations $\mathbf{r}_i$, $\mathbf{v}_i$ and $\mathbf{a}_i$ at a later time $t + \Delta t$ are calculated numerically by using finite difference algorithms such as equation 4.4.

4. The calculated properties are used as new input values, and this process continues until equilibrium is reached.

4.1.4 *Equilibration*

The numerical integration of Newton's equations brings the system from the initial, unrelaxed state towards an equilibrium state. Eventually, the net forces on each atom will be zero, and the system properties no longer changes with time. During this process, the potential energy is driven to its minimum value, while the total energy (sum of potential and kinetic energy) normally is kept constant. To reach this minimum potential energy state, the pressure and temperature of the system can be controlled by rescaling the velocities of the particles. The average kinetic energy $\langle E_{kin} \rangle$ is related to the average velocity of each atom and to temperature through the following equation,

$$\langle E_{kin} \rangle = \left\langle \frac{1}{2} \sum_i m_i v_i^2 \right\rangle = \frac{3}{2} N k_B T \tag{4.5}$$

where N is the total number of atoms and k_B is the Boltzmann constant. This means that the average velocity $\langle v \rangle$ is related to temperature as

$$\langle v \rangle = \left(\frac{3 k_B T}{m} \right)^{1/2} \propto T^{1/2} \tag{4.6}$$

The temperature of the system can therefore be changed from T to T' by multiplying the each component of the velocity by the same factor,

$$\langle v_{new} \rangle = \langle v_{old} \rangle \left(\frac{T'}{T} \right)^{1/2} \tag{4.7}$$

Equation 4.7 can be used to change the velocities of the atoms and therefore also the kinetic energy of the system.

Temperature control algorithms are normally referred to as thermostats, and can be divided into different categories based on how the rescaling of particle velocities is implemented. In *strong coupling methods*, the velocities of the particles are scaled to give the exact temperature, while in *weak coupling methods*, the velocities are only

modified in the direction of the desired temperature. In *stochastic methods*, the velocities of the particles are changed stochastically to match the velocity distribution function of the desired temperature, and *extended system methods* introduce an extra degree of freedom to include temperature. In this project, two different temperature control algorithms were used, the Langevin thermostat (stochastic) and the Nosé-Hoover thermostat (extended system).

4.1.5 *Langevin thermostat*

The Langevin thermostat is an example of a stochastic temperature control method, and can be implemented by using both the NVT and the NpT ensembles. It controls the temperature through a modification of Newton's equations, where a friction force and a random force is added to describe the viscous effect of a solvent [26]. This can be thought of as adding a sea of much smaller fictional particles surrounding the atoms being simulated. The friction force simulates the drag force on the solute atoms from the solvent, and the random force simulates the random collisions between the solvent particles and the solute.

The velocity v_i of each particle being simulated can be expressed as the time derivative of its position r_i,

$$\frac{dr_i}{dt} = \frac{p_i}{m_i}, \tag{4.8}$$

where the momentum p_i is calculated from the following differential equation:

$$\frac{dp_i}{dt} = F_i - \gamma_i p_i + f_i. \tag{4.9}$$

Here, F_i is the force on particle i due to interactions with other particles, γ_i is a friction coefficient and f_i is a random force generated from a Gaussian distribution with variance

$$\sigma_i^2 = 2m_i\gamma_i\frac{k_B T}{\Delta t}. \tag{4.10}$$

The time step Δt is the same time step used in the numerical integration of the equations of motion, and T is the goal temperature, so the adjustment of particle velocities will drive the system to this temperature over time.

4.1.6 *Nosé-Hoover thermostat*

The Nosé-Hoover thermostat is an example of a extended system method, and uses the NVT ensemble. Here, a heat bath is introduced

as an additional degree of freedom. This heat bath is regarded an integral part of the system, and is associated with a fictional "heat bath mass" Q controlling the coupling between the system and the heat bath [27]. In contrast to the Langevin thermostat, the temperature is adjusted without involving random numbers.

4.2 *ab initio* MOLECULAR DYNAMICS

Classical MD is typically extremely fast compared to first-principles methods such as DFT, but less accurate because the interatomic potentials are generated empirically. Typically, the force fields are parametrisations based on one specific experiment or scenario, and won't necessarily give an accurate description of the system in question. Also, no electromagnetic properties can be derived from classical MD since the electronic structure is not taken into account, and the time scale is limited to nanoseconds.

In *ab initio* molecular dynamics, the forces on each particle in the system are calculated by using first principles methods (quantum mechanics) instead of classical mechanics. This means that the electronic structure is explicitly taken into account, and the accuracy of the calculation is drastically increased compared to classical MD. However, this accuracy comes at the cost of a more computationally expensive simulation because the Schrödinger equation needs to be solved at each time step. *ab initio* MD is therefore often limited to small simulation cells and short time scales.

One way to speed up *ab initio* MD simulations is by using force fields, which are parametrisations of the potential energy. Also, these force fields can be generated by using machine learning, which will reduce the computational cost even further.

4.3 MACHINE LEARNING

Machine learning is a branch of computer science with focus on imitating the way the human brain works [28]. By using algorithms to build a model that learns from its experiences, one can make the computer do decisions and predictions it's not explicitly programmed to. A more formal definition of this learning process is

> *A computer program is said to learn from experience E with respect to some class of tasks T and performance measure P, if its performance at tasks in T, as measured by P, improves with experience E.* ([29])

Here, it is important to notice that the computer only learns from experience E if that improves its performance. In other words, the model is trained to become more and more accurate, as each adjustment only makes its performance better. Machine learning can be

used to solve a number of tasks, e.g. regression, classification and denoising [29].

4.3.1 *Machine learned force fields*

When machine learning is used to train force fields used in molecular dynamics simulations, this is a type of supervised machine learning. Supervised machine learning means that the model is trained on labeled data sets, where some input data already is tagged with the correct output [28]. The training data can be thought of as a supervisor for the model, with the labeled input data "teaching" the machine how to predict the correct output.

In this project, the machine learned force fields (MLFF) were generated by using an on-the-fly method, which means that they were trained during an *ab initio* MD simulation. This method is implemented in VASP, and has proven successful and efficient in the prediction of thermodynamic properties of anharmonic materials [30].

Figure 4.2 illustrates how these MLFFs are generated. First, any existing MLFFs are read in, before the *ab initio* MD simulation begins. Then, for each step in the simulation, the energy, forces and stress tensor as well as the Bayesian error estimate of forces (BEEF) are calculated. The BEEFs are estimates of the out-of-sample error, which is the average error occurring when the force fields trained so far are used to consider a new configuration from the same ensemble [31]. These error estimates are expected to become smaller and smaller during the training process, as the force fields learns how to describe the different configurations more and more accurately.

The Bayesian error estimate of forces are then used to determine whether a first principle DFT calculation is necessary for that step or not. If the error estimates are large, it means that the new configuration differs a lot from what VASP has learned so far, and a DFT calculation is used to describe that step. In that case, the first principle calculation is performed, and the machine learning model are updated with the resulting force fields. However, if the error estimates are small, the already existing force fields can be used to describe that step.

In the next step, the positions and velocities of all the particles in the system are then updated, either by using the old or the updated machine learning force fields. Then the simulation proceeds to the next step with predicting the energy, forces, stress tensor and Bayesian error estimate of forces of the new configuration. When the total number of steps is reached, the system properties and final machine learned force fields can be found in the output files.

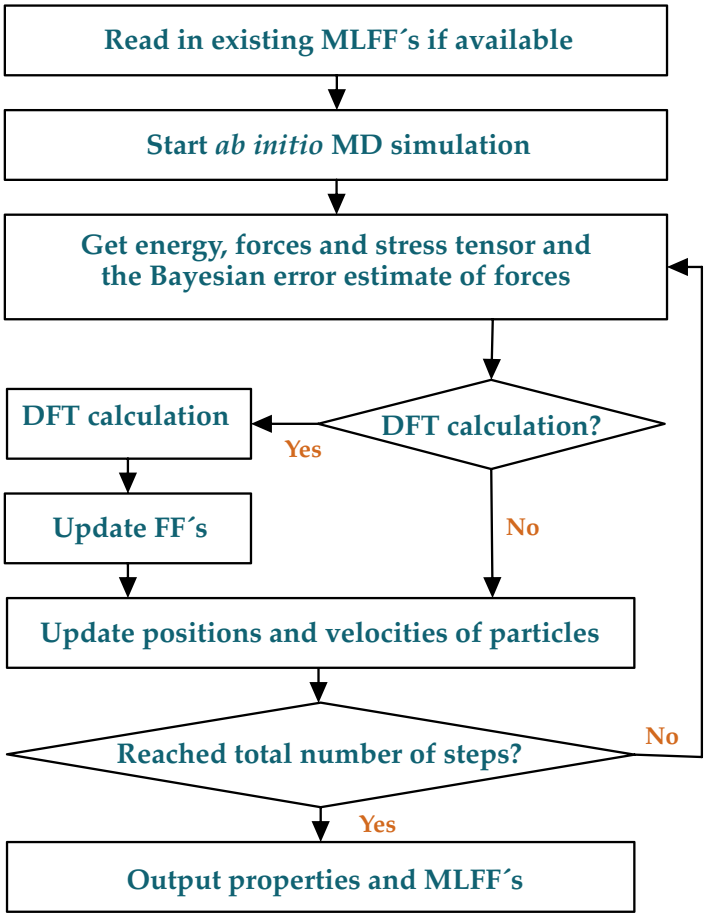

Figure 4.2: Flowchart describing how the machine learned force fields are trained on-the-fly, during a *ab initio* molecular dynamics simulation. Figure inspired by [32].

5 COMPUTATIONAL METHODS

In this project, the supercomputer Fram provided by UNINETT Sigma2 (the National Infrastructure for High Performance Computing and Data Storage in Norway) was used for all the DFT calculations. All DFT calculations were performed using VASP with the PBEsol functional and the Hubbard 'U' correction, with a 'U' value of 5.5 and an energy cutoff of 500 eV. Details about the convergence testing can be found in Appendix section C. The PBEsol + U functional was chosen due to successful results using this functional for prediction of the structural and electronic properties of the TMA[$FeCl_4$] and TMA[$FeBr_4$] crystals in previous work [2].

To predict the phase transitions and rotational dynamics of the two plastic crystals TMA[$FeCl_4$] and TMA[$FeBr_4$], *ab initio* molecular dynamics simulations with machine learned force fields (MLFFs) were performed. For the simulations of phase transitions, a Langevin thermostat (NpT ensemble) was used, while the Nosé-Hoover thermostat (NVT ensemble) was used for the analysis of the rotational dynamics of the crystals. With the Langevin thermostat the volume is variable, leading to displacements of atoms. When analysing the rotational dynamics the volume needs to be constant, which is why the Nosé-Hoover thermostat was chosen for this purpose. In both cases, the MLFFs were first generated and trained on-the-fly on a 2×2×2 supercell by using a Γ-centered k-point grid. The final potentials were then used in the phase transition- and rotational dynamics simulations.

5.1 GENERATION OF MLFF

The machine learned force fields (MLFFs) were generated on-the-fly, meaning that they were trained during an *ab initio* MD run. For each plastic crystal, the force fields were generated using the Langevin thermostat from 200 K to 400 K over a period of 40 ps. The generated machine learning force fields were then used for the production runs and for the rotational analysis using the Nose-Hoover thermostat at constant volume.

In previous work, it has been shown that different starting configurations of the two plastic crystals give similar results when it comes to predicting the structural and electronic properties of these compounds. This means that although the crystals theoretically have a large number of possible configurations due to the rotational freedom of the TMA molecules, the different configurations are equivalent as a basis for predicting material properties trough DFT simulations [2].

In this thesis, the same starting configuration was used for all force field calculations.

Using the Langevin thermostat, the force fields were generated by first equilibrating the structures at 200 K, then heating them up from 200 K - 400 K, followed by a new equilibration at 400 K. In this way, all possible configurations between 200 K and 400 K would theoretically be captured by the final force fields. The simulations were run for 20,000 steps with a time step of 2 fs per step, giving a total simulation time of 40 ps.

In calculations using the Langevin thermostat, an appropriate value of the friction coefficient γ_i (see equations 4.9 and 4.10) also needs to be determined. This friction coefficient represents the atomic degrees-of-freedom (in units of ps^{-1}) and is specified through the `LANGEVIN_GAMMA` tag in the `INCAR` files. In addition, a friction coefficient `LANGEVIN_GAMMA_L` (in ps^{-1}) and a fictitious mass `PMASS` (in amu) for the lattice degrees-of-freedom needs to be specified when a NpT ensemble is used. In this project, the atomic friction coefficient `LANGEVIN_GAMMA` was only set to non-zero for the hydrogen atoms, and four different values were investigated (0, 1, 2 and 5). For each of these, four different values of the lattice friction coefficient `LANGEVIN_GAMMA_L` were tested (0, 1, 5 and 10). Based on the performance of the different parameter combinations, the total run-time for the simulations and inspections of the final structures in VESTA [33], both `LANGEVIN_GAMMA` and `LANGEVIN_GAMMA_L` were set to 5.

A complete overview of the `INCAR` parameters used for the generation of MLFFs can be found in Appendix section A (see listing A.1).

5.2 PREDICTING PHASE TRANSITIONS

With the final machine learned force fields, the two plastic crystals were first slowly heated from 200 K to 400 K, then cooled down from 400 K to 100 K. The reason for this asymmetric temperature treatment was to capture all phase transitions listed in table 2.2 during the cooling process. The starting configuration for both plastic crystals was the ferroelectric Amm2 phase, which corresponds to a temperature of about 330 K. During the heating process from 200 K to 400 K, a phase transition to the plastic $Pm\bar{3}m$ mesophase via the Cmcm phase was expected (see table 2.2). As mentioned in section 2.3.1, it is important to remember that whilst this mesophase is assigned the $Pm\bar{3}m$ space group, most of the symmetry is broken at this point due to the extreme rotational disorder. During the cooling process from 400 K to 100 K, the goal was to observe phase transitions both from the $Pm\bar{3}m$ phase back to the Amm2 phase ($Pm\bar{3}m \rightarrow$ Cmcm $\rightarrow$ Amm2), but also the further transitions down to the Pbcm phase (Amm2 $\rightarrow$ Pma2 $\rightarrow$ Pbcm). As shown in table 2.2, the Pbcm phase corresponds to a temperature of about 250 K.

The phase transitions, both during the heating and cooling simulations, were observed by tracking the lattice parameters (a, b, c), the unit cell volume and the total energy of the TMA[$FeCl_4$] and TMA[$FeBr_4$] crystals. These quantities can be retrieved from the `XDATCAR` and `OSZICAR` output files.

The slow heating and cooling simulations were run for 400,000 steps with a time step of 2 fs per step, giving a total simulation time of 800 ps each (1600 ps for both heating and cooling). The `INCAR` parameters for these calculations are presented in listing A.2.

5.2.1 *Generation of Simulated XRD data*

From the `XDATCAR`s, the X-ray diffraction (XRD) spectra for the plastic crystals were also generated, by using the Pymatgen package in python [34]. By computing the XRD pattern for each structure at each time step, one can see how the diffraction pattern changes upon heating and cooling, indicating where the phase transitions take place. The `XRDCalculator` from the `pymatgen.analysis.diffraction.xrd` module was used with a wavelength of 0.730 74 Å, in order to match the wavelength used in previous experiments conducted by Walker *et al* [35]. Walker *et al* conducted the XRD experiments at the Swiss Norwegian Beam Lines (SNBL), beam line BM01, European Synchrotron Radiation Facility (ESRF). A Pilatus 2M detector was used with a wavelength of 0.730 74 Å [35]. Although Walker *et al* investigated the plastic crystal TMA[$FeBrCl_3$], the same wavelength was used in the analysis of TMA[$FeCl_4$] and TMA[$FeBr_4$] in this project for comparison reasons, as these crystals have the same structure and the only difference between them is the choice of halogens used in the inorganic anions. The simulated XRD patterns were averaged every 100'th step to smoothen the spectrum and to give the effect of an averaged structure.

5.3 ROTATIONAL DYNAMICS

The rotational dynamics of the two plastic crystals [TMA][$FeCl_4$] and [TMA][$FeBr_4$] was studied at three different temperatures: 200 K, 300 K and 400 K. In these calculations a Nosé-Hoover thermostat was used, and the calculations were run for 50,000 steps over a time period of 100 ps.

From these calculations, an autocorrelation function was used to analyse the rotations of the organic TMA cations in each crystal. The autocorrelation function provides information about how much a structure correlates with itself at a previous time step. Analysing the correlation over time gives a good indication of the rotational freedom of the molecules, as more rotational freedom is associated

with less correlation between structures at different time steps in the simulation.

As mentioned in section 2.3.1, the rotational disorder in the plastic crystals TMA[$FeCl_4$] and TMA[$FeBr_4$] is mainly due to the rotations of the globular TMA molecules, as the positions of the inorganic anions $[FeCl_4]^-$ and $[FeBr_4]^-$ are relatively well defined. Therefore, the rotational dynamics of the two crystals were only investigated by analysing the rotations of the TMA molecules.

As figure 5.1 shows, the rotational autocorrelation $C(t)$ is calculated by defining an "up" vector $\mathbf{P}_i$ for the initial configuration, and then determining the angle θ of each subsequent structure N relative to that initial configuration. The angle θ is found by taking the dot product of the "up" vector at the initial time step t_0, $\mathbf{P}_i(t_0)$, and the rotated "up" vector at a later time t, $\mathbf{P}_i(t)$. The autocorrelation function $C(t)$ can then be defined by

$$C(t) = \langle \mathbf{P}_i(t_0) \cdot \mathbf{P}_i(t) \rangle_{t_0,i} \tag{5.1}$$

This method have previously been used with success by e.g. Yoneya *et al* [10].

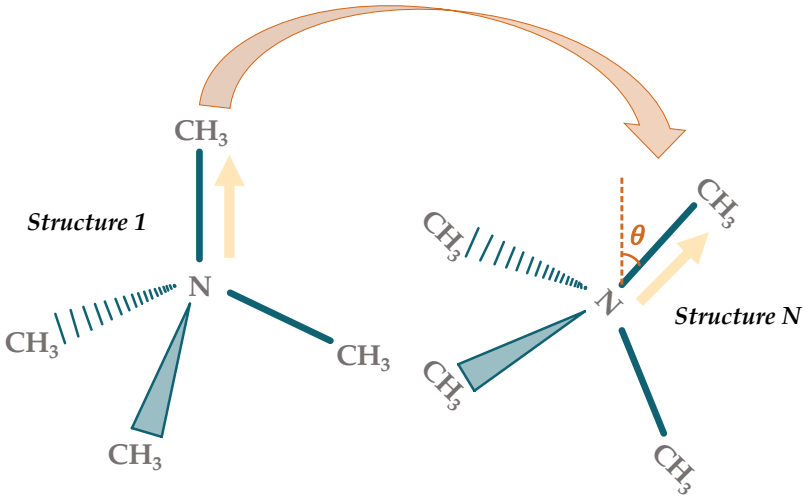

Figure 5.1: Rotation of tetramethylammonium (TMA) molecule, where one methyl group have been defined as "up" and the orientations of the following structures relative to the initial one can be determined by tracking this "up" methyl group and calculating the angle θ between them.

When calculating the correlation between structures in a dataset that are k time periods apart, the autocorrelation is said to be a lag k autocorrelation. Structures that are close in time will have a higher correlation than structures far apart in the dataset, and determining the optimal lag value is therefore important. In this project, four different lag values were tested: 50, 100, 150 and 200. A lag value

of 100 was chosen as this was the largest one with the whole curve outside the cone representing the 95% confidence level. The results from this testing can be found in Appendix section B.

6 RESULTS

This chapter presents the results from the DFT calculations, including Bayesian error estimate of forces (BEEF) plots from the generation of MLFFs, lattice parameters for the plastic crystals during the heating and cooling simulations, XRD spectra and analysis of the rotational dynamics of TMA[$FeCl_4$] and TMA[$FeBr_4$].

6.1 GENERATION OF MACHINE LEARNED FORCE FIELDS

Figure 6.1 shows the Bayesian error estimate of forces (BEEF) as a function of time for the generation of the machine learned force fields (MLFF) from 200 K to 400 K. This was the middle step of the force field generation, after the 200 K equilibration and before the 400 K equilibration. The BEEF plots for the 200 K to 200 K and the 400 K to 400 K calculations can be found in Appendix section D.

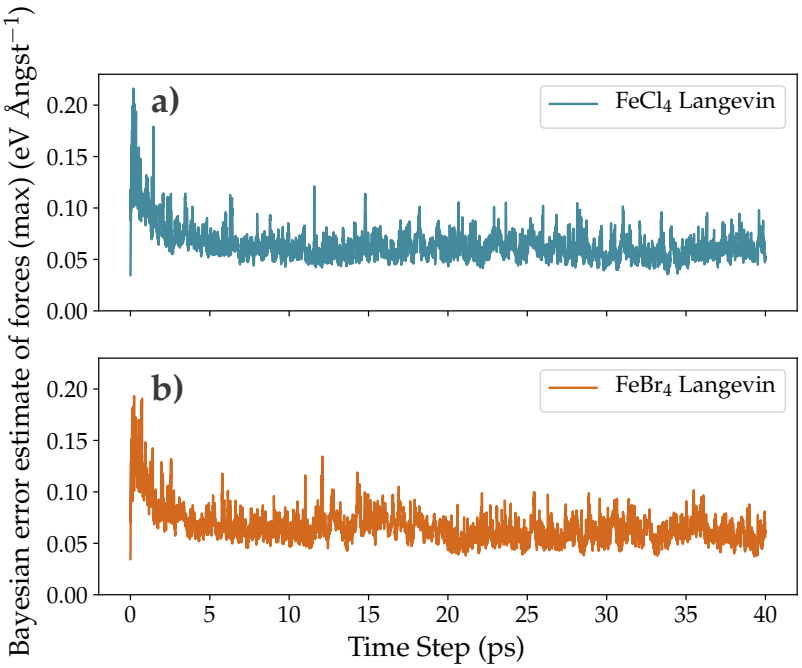

Figure 6.1: Bayesian error estimate of forces for the generation of MLFFs from 200 K to 400 K, for a) TMA[$FeCl_4$] and b) TMA[$FeBr_4$].

As described in section 4.3.1, the Bayesian error estimate of forces are the uncertainties used to determine whether or not to do a first principle calculation during the MD simulation used to train the machine learned force fields (MLFF). Any big spikes in the BEEF plot indicates that the force fields meets a configuration that differs a lot

from what VASP has learned so far, meaning that a first principle calculation is necessary to describe that step. From figure 6.1, it is clear that the error estimates are biggest in the beginning of the simulation, which is as expected because the training process just have started and the force fields have only learned to describe a small number of configurations. As the simulation continues, the error estimates becomes smaller and smaller, meaning that the force fields gets better and better at describing unknown configurations. An important note is that the Bayesian error estimate of forces are only error estimates, not a direct indication of the quality of the MLFFs [31]. However, the BEEF plot gives a good indication of the progress of the training process. Ideally, the errors should be smaller than 0.1 eV, which is the case for both TMA[$FeCl_4$] and TMA[$FeBr_4$] at the end of the MLFF generation.

The ultimate validation of these force fields is how well they can predict the crystal properties described in literature from real experiments.

Figure 6.2 and 6.3 shows the total energy and temperature as a function of time for the generation of the machine learned force fields (MLFF)s from 200 K to 400 K, respectively. The temperature increases gradually from 200 K to 400 K as expected, and there is a strong correlation between the total energy and the temperature. This can be seen from the fact that the energy and temperature curves for each crystal are almost identical in shape.

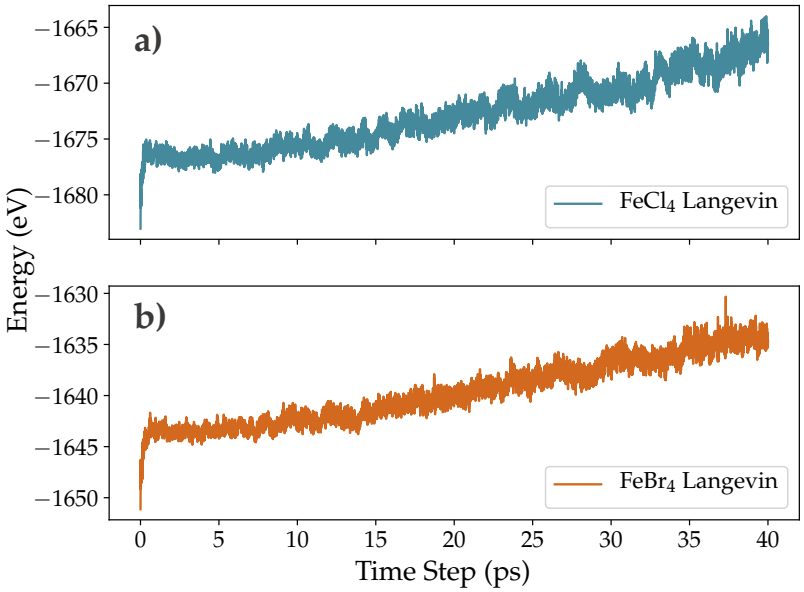

Figure 6.2: Total energy for the generation of MLFFs from 200 K to 400 K for a) TMA[$FeCl_4$] and b) TMA[$FeBr_4$].

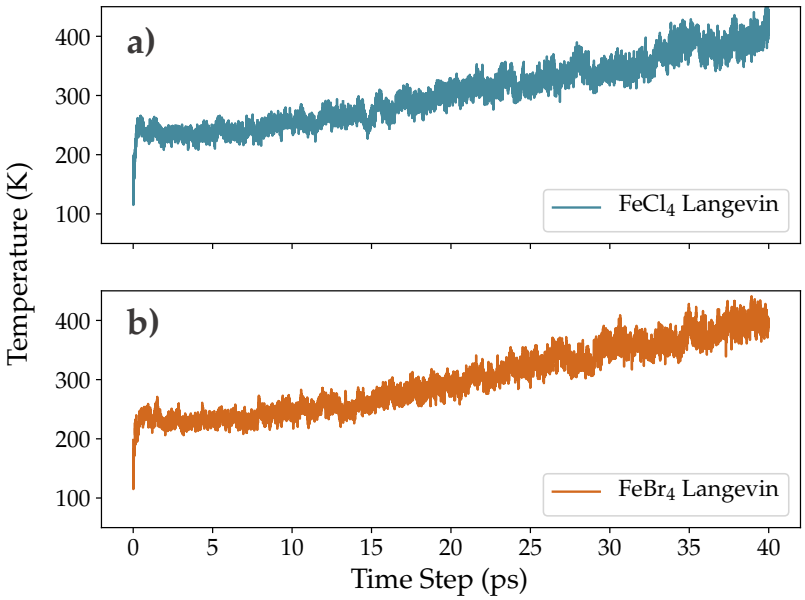

Figure 6.3: Temperature change during the generation of MLFFs from 200 K to 400 K for a) TMA[$FeCl_4$] and b) TMA[$FeBr_4$].

6.2 PREDICTING PHASE TRANSITIONS

The phase transitions of the two plastic crystals were studied by tracking the lattice parameters, unit cell volume and total energy from the slow heating (200 K to 400 K) and cooling (400 K to 100 K) simulations, over a time frame of 1600 ps in total. The XRD spectra for the two crystals were also generated, and plotted as a function of time step.

6.2.1 *Lattice parameters and total energy*

Figure 6.4 shows the unit cell volume, lattice parameters and temperature as a function of step number for the heating process of the two plastic crystals. The column to the left are the results for the TMA[$FeCl_4$] crystal, while the column to the right gives the results for TMA[$FeBr_4$]. The two vertical black lines in each figure corresponds to temperatures where phase transitions are expected, based on experimental results. In 2018, Harada *et al* reported the crystal data and temperatures for five different phases of the TMA[$FeCl_4$] compound (see table 2.2), including the transition from the ferroelectric Amm2 phase to the Cmcm phase at 360 K and the transition from the Cmcm phase to the cubic $Pb\bar{3}m$ phase at 400 K [20]. In figure 6.4, the vertical black lines corresponds to the points in time where the temperature exceeds 360 K and 400 K. The dark blue and dark red lines in each plot are the smoothened curves over every 1000 steps.

Figure 6.5 shows the unit cell volume, lattice parameters and temperature as a function of time step for the slow cooling of the two

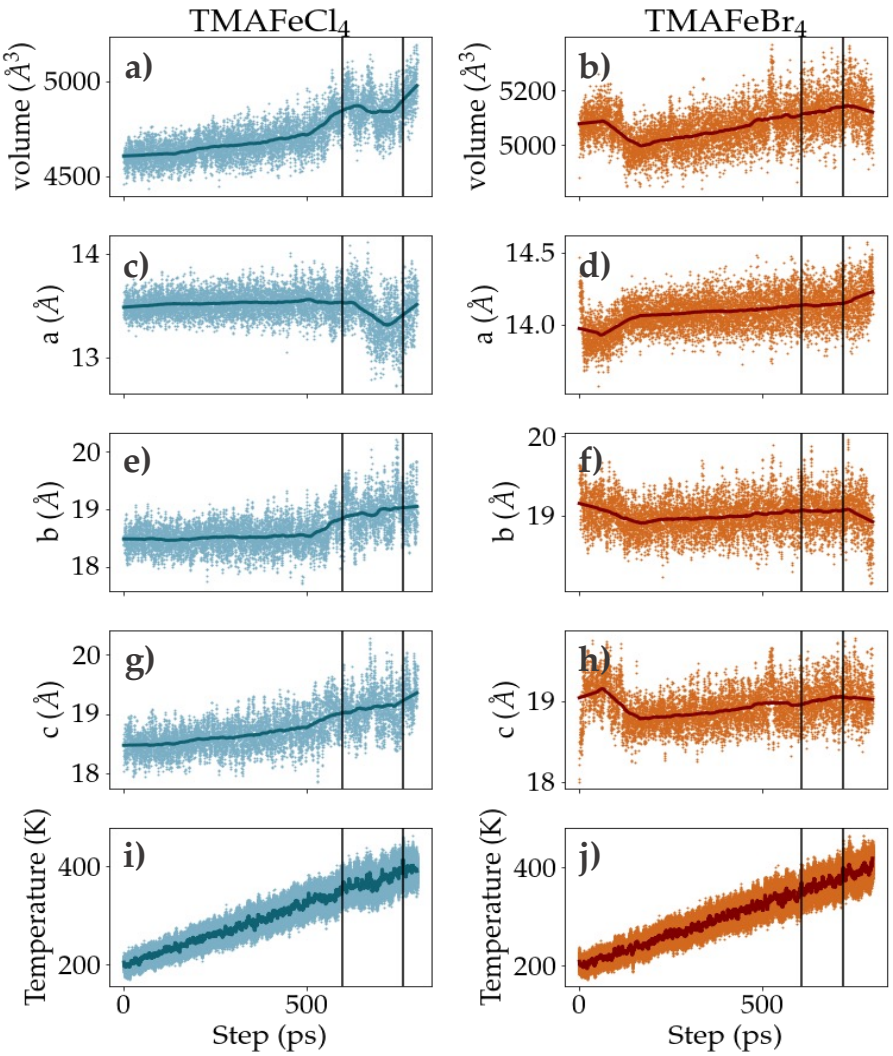

Figure 6.4: Change in lattice parameters during the heating process from 200 K to 400 K. The figures to the left correspond to TMA[$FeCl_4$] and the figures to the right correspond to TMA[$FeBr_4$]. Figure a) and b) shows the volume change for TMA[$FeCl_4$] and TMA[FeBr], respectively, and figure c) - h) shows the change in the individual lattice parameters a, b and c. Figure i) and j) shows the temperature change during the simulation for TMA[$FeCl_4$] and TMA[FeBr], respectively. The dark blue and dark red lines are the averaged values of the various properties, and the two vertical black lines in each plot corresponds to temperatures of 360 K and 400 K, which is where the phase transitions are expected to occur according to literature [20].

plastic crystals. The column to the left gives the TMA[$FeCl_4$] results and the column to the right gives the TMA[$FeBr_4$] results. As in figure 6.4, the black vertical lines corresponds to temperatures where phase transitions are expected to happen in the TMA[$FeCl_4$] crystal (see table 2.2). From left to right, these four temperatures are 360 K, 330 K,

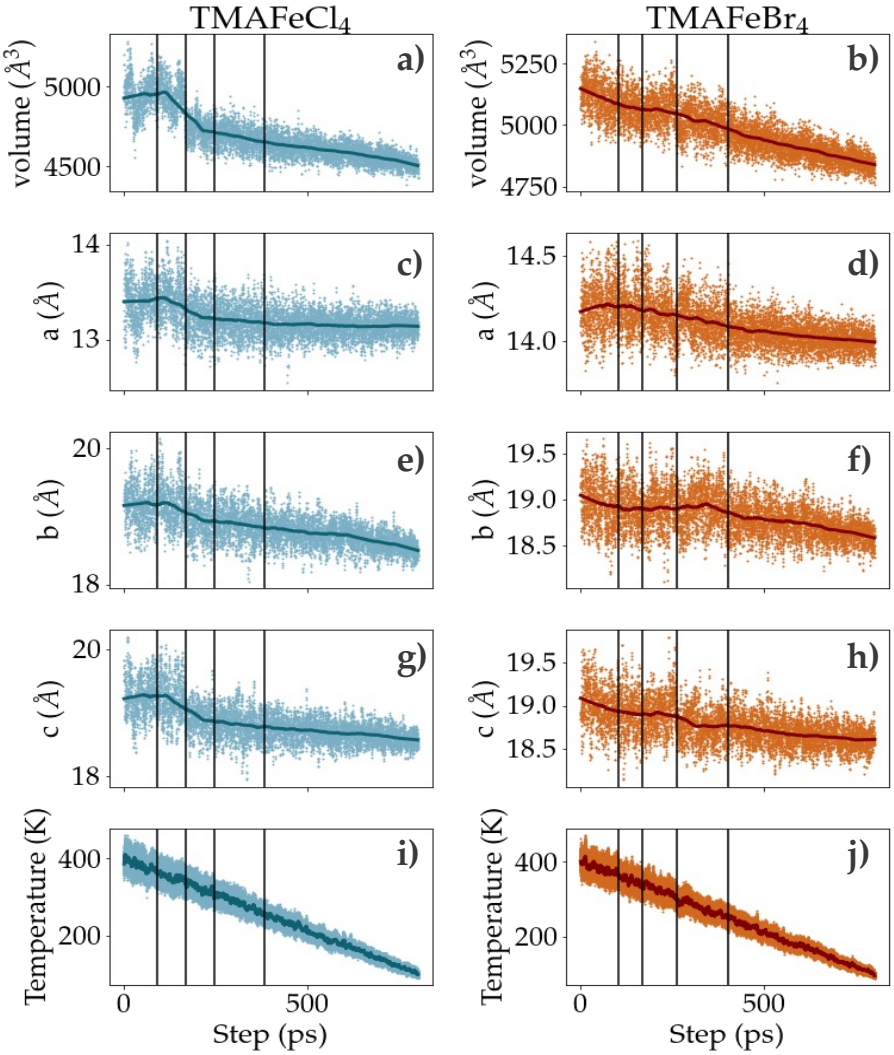

Figure 6.5: Change in lattice parameters during the cooling process from 400 K to 100 K. The figures to the left correspond to TMA[$FeCl_4$] and the figures to the right correspond to TMA[$FeBr_4$]. Figure a) and b) shows the volume change for TMA[$FeCl_4$] and TMA[FeBr], respectively, and figure c) - h) shows the change in the individual lattice parameters a, b and c. Figure i) and j) shows the temperature change during the simulation for TMA[$FeCl_4$] and TMA[FeBr], respectively. The dark blue and dark red lines are the averaged values of the various properties, and the four vertical black lines in each plot corresponds to temperatures of 360 K, 330 K, 300 K and 250 K, which is where the phase transitions are expected to occur according to literature [20].

300 K and 250 K corresponding to the transitions to the phases Cmcm, Amm2, Pma2 and Pbcm, respectively.

For TMA[$FeCl_4$], figure 6.4 a) and c) clearly shows that there is an increase in the unit cell volume, accompanied by a decrease in the lattice parameter a at 360 K. Figure 6.4 e) and g) shows that both the lattice parameters b and c increases at this temperature, but the

change in the slope is most prominent for b. At 400 K, there is a new volume increase for the TMA[$FeCl_4$] crystal. Here, lattice parameter a starts to increase, together with a small increase of b and c. The temperature curve in figure 6.4 i) increases gradually from 200 K to 400 K, as expected.

When it comes to the cooling process for TMA[$FeCl_4$], figure 6.5 a) clearly shows that there is a volume change in the beginning of the simulation, between 360 K and 300 K. This volume decrease is accompanied by a decrease in the lattice parameters a, b and c. For the rest of the simulation, the lattice parameters continues to decrease, but with a slightly flatter slope. The temperature decreases gradually from 400 K to 100 K, with no big spikes or deviations.

For the TMA[$FeBr_4$] crystal, figure 6.4 shows that there is a change in the unit cell volume and lattice parameters early in the heating process, in contrast to the TMA[$FeCl_4$] crystal. From figure 6.4 b), d), f) and h), it is clear that the unit cell volume and lattice parameters b and c decreases after only a couple of picoseconds, while the lattice parameter a starts to increase. This is followed by a slight increase in both the volume, a, b and c throughout the rest of the simulation, with no significant changes around the 360 K line. After the second vertical line at 400 K, there is a small increase in the slope of the lattice parameter a, while the volume, b and c starts to decrease. The temperature graph in figure 6.4 j) is similar to the temperature development for the TMA[$FeCl_4$] crystal, with only a minor bump around the 300 K line.

For the cooling process of the TMA[$FeBr_4$] crystal, figure 6.5 b) shows that the unit cell volume decreases gradually throughout the simulation, with few fluctuations or pronounced variations. The lattice parameters a, b, and c also have few significant changes, but there are some interesting areas around the vertical black lines. Between the 400 K and 360 K line, lattice parameter a seems to increase slightly, followed by a decreasing trend after 360 K (figure 6.5 d)). The lattice parameters b and c also have a small change in the slope around the 360 K, where the graph flattens out a bit before it stars decreasing again between 300 K and 250 K. The temperature (figure 6.5 j)) show a small fluctuation around 300 K, but besides that it decreases gradually from 400 K to 100 K as expected.

Figure 6.6 and 6.7 shows how the total energy per atom changes during the heating and cooling process, respectively. The temperature plots are also included, together with the vertical black lines indicating where phase transitions are expected to happen. In figure 6.6, the two lines indicates where the temperature exceeds 360 K and 400 K (from left to right), and in figure 6.7 the four lines indicates where the temperature drops below 360 K, 330 K, 300 K and 250 K (from left to right).

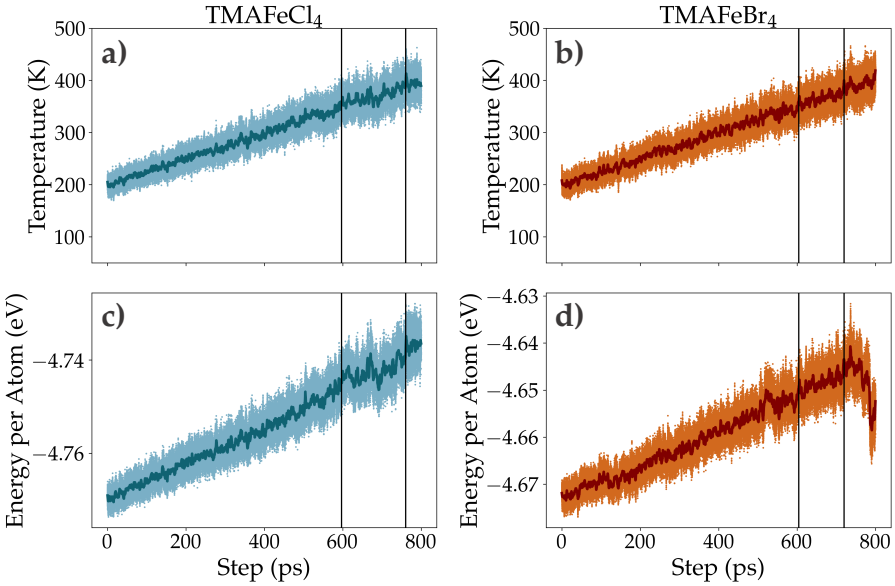

Figure 6.6: Temperature and energy per atom for the heating of the two plastic crystals from 200 K to 400 K. The TMA[$FeCl_4$] crystal is to the left and the TMA[$FeBr_4$] to the right.

For the TMA[$FeCl_4$] crystal, figure 6.6 c) shows that the energy per atom correlates well with the increasing temperature. However, there are small energy fluctuations between 360 K and 400 K suggesting that a phase transition occurrs in this region. For the cooling process, figure 6.7 c) shows the same stable trend with decreasing energy, but with small fluctuations around 360 K and 330 K.

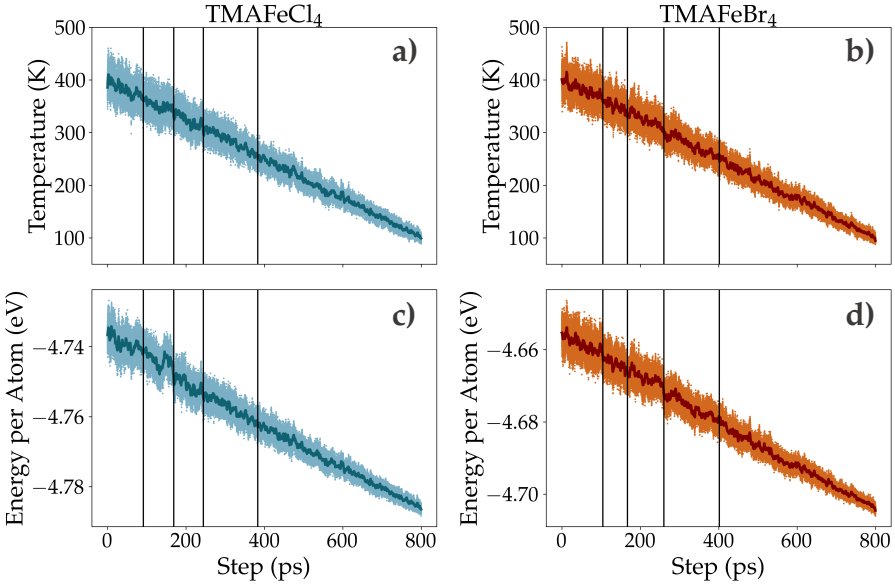

Figure 6.7: Temperature and energy per atom for the cooling process from 400 K to 100 K. The TMA[$FeCl_4$] crystal is to the left and the TMA[$FeBr_4$] to the right.

For TMA[$FeBr_4$], figure 6.6 d) shows that there is a small shift in the energy after a few picoseconds, but besides from that the energy per atom increases gradually with few fluctuations up to the 400 K line. However, after crossing this line, the energy per atom seems to drastically decrease for the rest of the simulation, although the temperature continues to increase. When it comes to the cooling of TMA[$FeBr_4$], figure 6.7 shows a better correlation between the energy per atom and temperature, and the energy decreases steadily with only minor fluctuations around 330 K.

Determination of the space group symmetry in a highly mobile finite size cell is difficult, and a reduced superstructure consisting of only Fe atoms was therefore formed for the two plastic crystals TMA[$FeCl_4$] and TMA[$FeBr_4$] in order to circumvent this. From these structures, rough symmetry information was obtainable, presented in figure 6.8 and 6.9. Here, the y-axes represent the lengths of the lattice parameters a, b and c, where the largest values correspond to the side lengths of the 2×2×2 supercell, and lower values (when obtainable) corresponds to the lengths of the roughly constructed unit cells by using symmetry elements. The x-axes gives the time step in picoseconds for the combined heating and cooling processes.

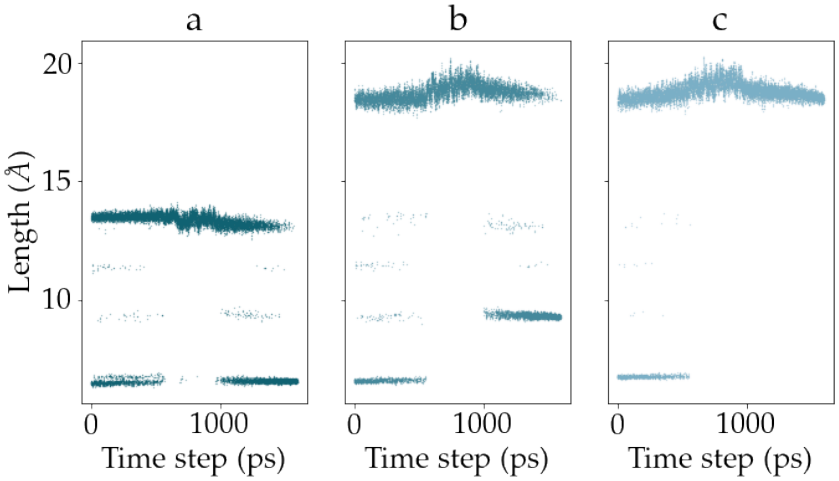

Figure 6.8: Reconstructed lattice parameters for the TMA[$FeCl_4$] crystal, showing where symmetry elements can be used to construct the lattice parameters for a single unit cell.

6.2.2 *Simulated XRD Spectra*

Figure 6.10 shows the XRD spectrum for the TMA[$FeCl_4$] crystal and how it changes during the heating and cooling processes. The equivalent spectrum for TMA[$FeBr_4$] is presented in figure 6.11. The y-axes of these plots represent time in picoseconds (ps), enabling the ob-

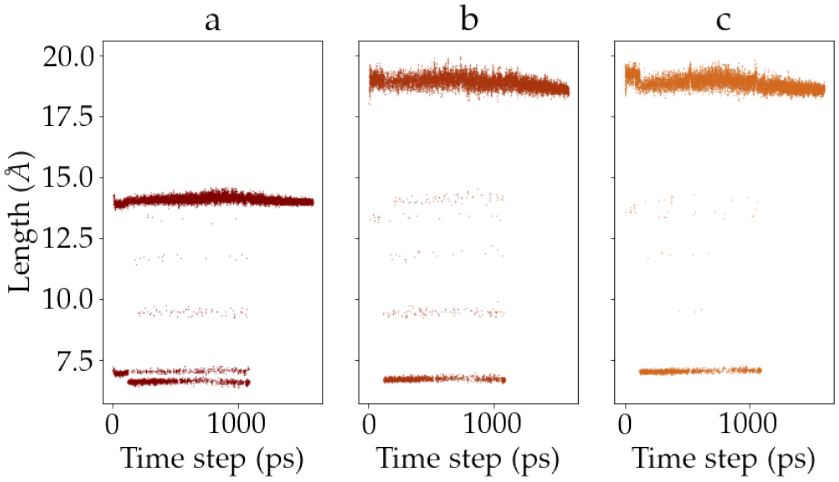

Figure 6.9: Reconstructed lattice parameters for the TMA[$FeBr_4$] crystal, showing where symmetry elements can be used to construct the lattice parameters for a single unit cell.

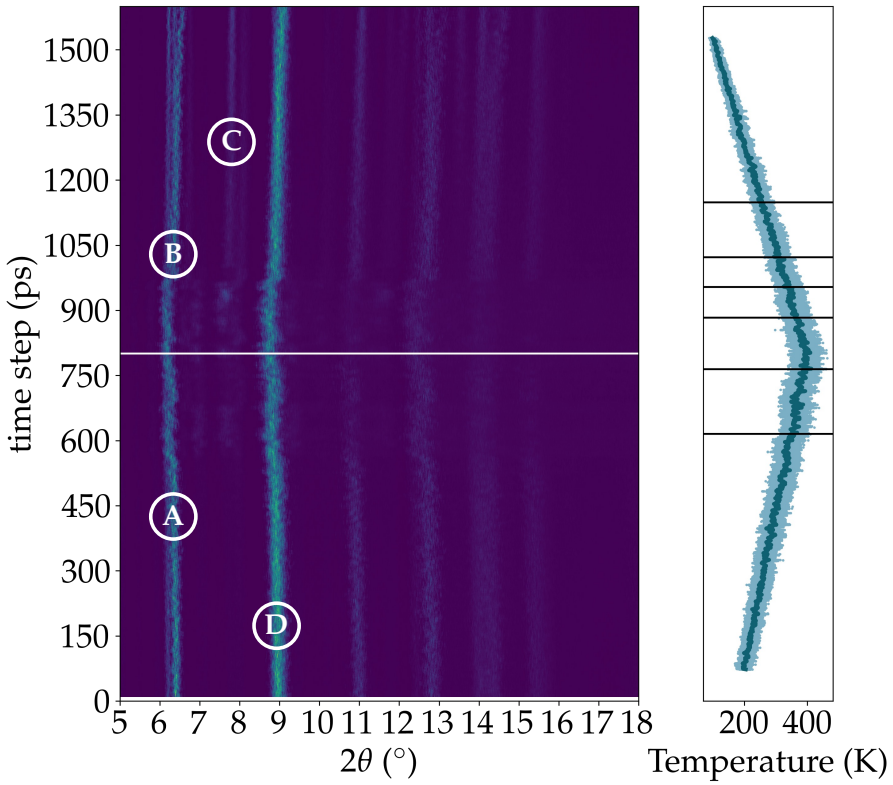

Figure 6.10: Simulated XRD spectrum for the TMA[$FeCl_4$] crystal. The y-axis gives the time step in ps, showing how the XRD lines changes during the heating and cooling processes. The plot to the right shows the corresponding temperature change from 200 K to 400 K and from 400 K to 100 K.

servation of the dynamic changes in the XRD lines throughout the simulations. The color map intensity corresponds to the intensity of the XRD peaks. The plots to the right of each figure shows the temperature change throughout the heating and cooling processes, first from 200 K to 400 K and then from 400 K back to 100 K.

For TMA[$FeCl_4$], there are a splitting of lines in the beginning of the heating process at about 6.2° 2θ and 6.4° 2θ, which merges into one single line at a critical point denoted A (see figure 6.10). Point A corresponds to a temperature of approximately 360 K. Subsequently, there is an observable bending of the XRD line in the high temperature area, shifting towards a lower 2θ values. At point B, there is a re-splitting of this line, accompanied by a bending back to higher 2θ values. Point B corresponds to a temperature of about 360 K, and the splitting becomes more pronounced as the crystal cools down to lower temperatures. During the cooling process, there also appears a new spectrum line at point C. This line corresponds to about 8° 2θ, and appears when the temperature have dropped below 250 K.

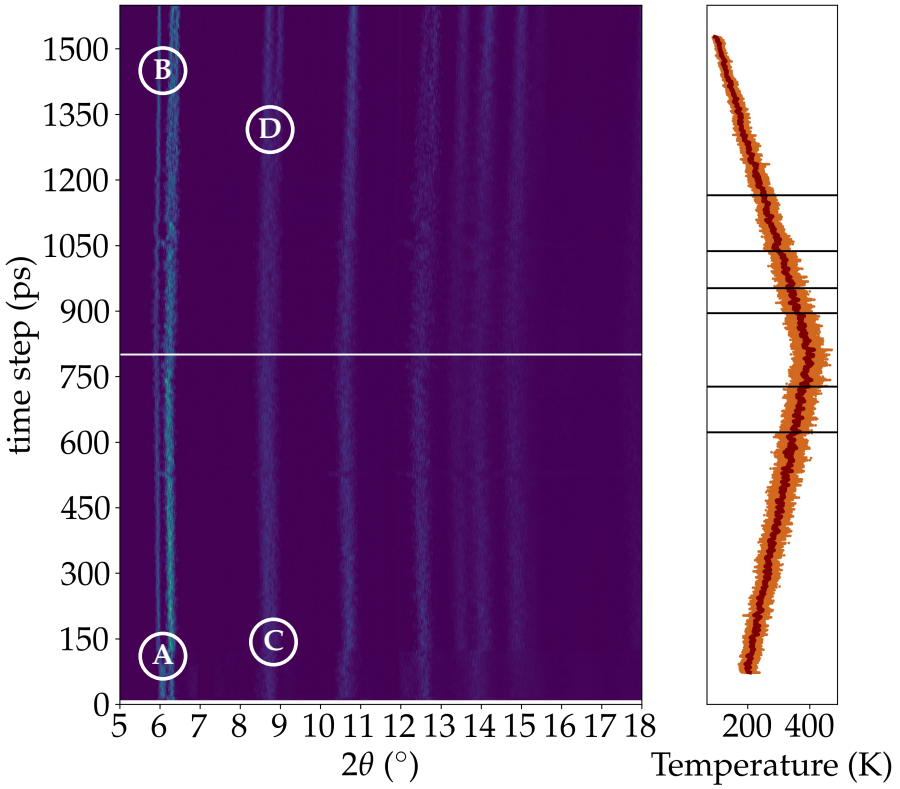

Figure 6.11: Simulated XRD spectrum for the TMA[$FeBr_4$] crystal. The y-axis gives the time step in ps, showing how the XRD lines changes during the heating and cooling processes. The plot to the right shows the corresponding temperature change from 200 K to 400 K and from 400 K to 100 K.

In addition, the TMA[$FeCl_4$] crystal have a peak around 9.0° 2θ (see point D). This line doesn't split up, but shows the same bending tendency towards lower 2θ values in the high temperature area.

In the case of the TMA[$FeBr_4$] crystal, there is a splitting of lines at approximately 6.0° 2θ and 6.3° 2θ, similar to those observed in the XRD plot for the TMA[$FeCl_4$] crystal. The gap between the split lines is slightly larger for the TMA[$FeBr_4$] crystal than for the TMA[$FeCl_4$] crystal, in addition to being shifted to lower 2θ values. In the high temperature area, there is a subtle bending of the lines as seen in the TMA[$FeCl_4$] crystal, but they does not merge together. On the contrary, the spacing between the lines appears to increase slightly during the cooling process, and at point B the two lines correspond to about 6.0° 2θ and 6.4° 2θ. The TMA[$FeBr_4$] crystal also have a XRD line at about 8.8° 2θ (point C). This line bends slightly towards lower 2θ values in the high temperature area, before it splits up at point D. This splitting of lines occurs almost in the end of the simulation, at a temperature between 250 K and 200 K.

6.3 ROTATIONAL DYNAMICS

Figure 6.12 shows the lag 100 autocorrelation function for the two plastic crystals at 200 K, 300 K and 400 K. The autocorrelation function was calculated by tracking one methyl group on each TMA molecule, as indicated by the grey arrow in the figure. More correlation within a crystal means that the structures at subsequent time steps are more similar, indicating that the TMA molecules don't rotate freely.

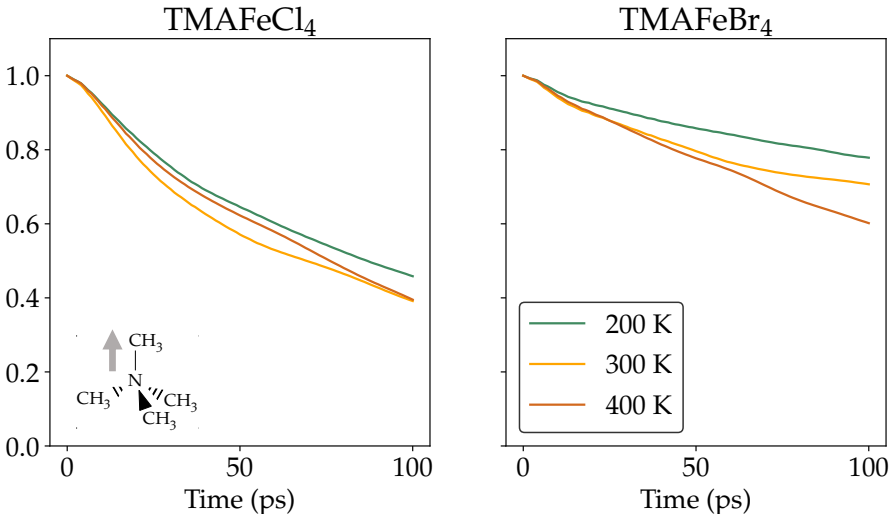

Figure 6.12: Autocorrelation function for the two plastic crystals TMA[$FeCl_4$] and TMA[$FeBr_4$] at three different temperatures, 200 K, 300 K and 400 K, with a lag value of 100. The grey arrow next to one of the methyl groups on the TMA molecule defines the axis for the calculation of the autocorrelation.

For TMA[$FeCl_4$], figure 6.12 shows that there is a higher correlation between the structures in the 200 K dataset within the time frame of 100 ps than for the structures in the 300 K and 400 K datasets. Also, the 300 K and 400 K phases appears to have almost the same degree of rotational freedom.

From figure 6.12, it is also clear that the TMA[$FeBr_4$] structure correlates more than the TMA[$FeCl_4$] structure, by doing a pairwise comparison of the 200 K, 300 K and 400 K phases for the two crystals. In the TMA[$FeBr_4$] crystal, the autocorrelation is clearly highest for the 200 K phase and lowest for the 400 K phase.

Figure 6.13 and 6.14 shows the trajectories of the tracked methyl groups used to calculate the rotational autocorrelation functions for TMA[$FeCl_4$] and TMA[$FeBr_4$], respectively. For the TMA[$FeCl_4$] crystal, figure 6.13 shows that there is more movement of the methyl groups in the 300 K and 400 K phases than in the 200 K phase. There are no significant differences between the 300 K and 400 K plot. For the TMA[$FeBr_4$] crystal, figure 6.14 shows a more gradually increase of rotational freedom, where there clearly is most movement in the 400 K phase and least movement in the 200 K phase.

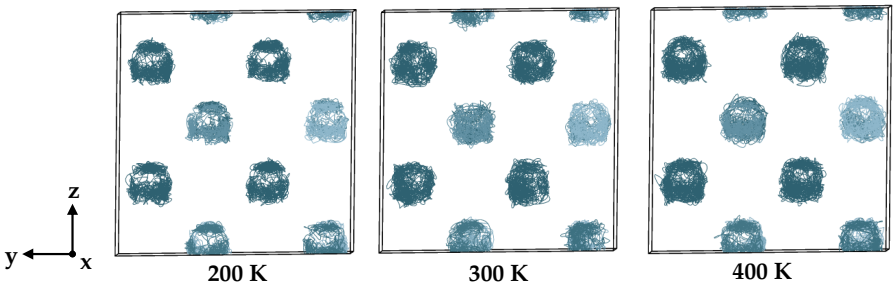

Figure 6.13: Trajectories of the tracked methyl groups used to calculate the autocorrelation function for the TMA[$FeCl_4$] crystal at 200 K, 300 K and 400 K.

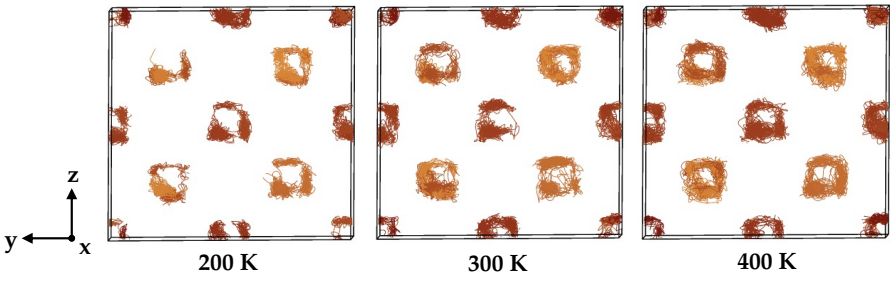

Figure 6.14: Trajectories of the tracked methyl groups used to calculate the autocorrelation function for the TMA[$FeBr_4$] crystal at 200 K, 300 K and 400 K.

7 DISCUSSION

In this thesis, the phase transitions and rotational dynamics of the plastic crystals TMA[$FeCl_4$] and TMA[$FeBr_4$] were studied. The main findings are discussed in the following section by first considering the phase transitions and how these can be observed through changes in lattice parameters and XRD spectra, followed by an analysis of the rotational dynamics within each structure. Lastly, some suggestions for further work are presented.

7.1 PHASE TRANSITIONS IN PLASTIC CRYSTALS

The phase transitions in the plastic crystals TMA[$FeCl_4$] and TMA[$FeBr_4$] were studied by looking at the change in lattice parameters, unit cell volume, energy per atom and the XRD spectra upon heating and cooling. The goal was to gain a deeper insight and understanding of how these materials work on a microscopic level, and how the differences in chemical composition affect the properties of the crystals.

7.1.1 *Lattice parameters*

In figures 6.4 – 6.7, the vertical black lines indicates where phase transitions were expected in two plastic crystals based on experimental data. These reference temperatures were retrieved from a paper by Harada *et al* in 2018, where the unit cell parameters a, b and c and the unit cell volumes for the different phases of the TMA[$FeCl_4$] crystal also were reported [20]. These crystallographic data are summarised in table 7.1. Although Harada *et al* studied the same plastic crystal TMA[$FeCl_4$] as investigated in this project, an important note here is that the plastic crystals studied in this project were simulated by using a $2\times2\times2$ supercell, while the experimental data in table 7.1 are averaged values retrieved from bulk materials. Comparing the size of the simulation cell used in this project with the defined literature values in table 7.1 is therefore not straightforward. However, the data in table 7.1 gives a good indication of the relative lengths of the lattice parameters for the different space groups, and how the unit cell volume can be expected to change upon heating and cooling.

Also, it is important to keep in mind that in real experiments, the long-range order and disorder in plastic crystals is captured, while DFT calculations captures the short-range behaviour of the crystals by using relatively small simulation cells. Although this short-range behaviour is extrapolated to imitate larger systems by the use of

periodic boundary conditions (PBC), predicting the true long-range behaviour and unordered nature of plastic crystals is a computational demanding task. Nevertheless, this thesis aims for predicting the phase transitions of these materials and get a better understanding of the mechanisms behind the rotational dynamics.

Table 7.1: Overview of the lattice parameters and unit cell volume for the five different space groups of TMA$FeCl_4$. Retrieved from [20].

Phase	V	IV	III	II	I
Temperature (K)	250	300	330	360	400
Space group	Pbcm	Pma2	Amm2	Cmcm	$Pm\bar{3}m$
a (Å)	6.44	14.27	7.22	8.96	6.81
b (Å)	13.07	6.44	9.02	9.62	6.81
c (Å)	14.00	6.45	9.36	14.16	6.81
V ($Å^3$)	1179	593	609	1221	316

Figure 6.4 shows the change in lattice parameters and unit cell volume for the plastic crystals during the heating from 200 K to 400 K. For the TMA[$FeCl_4$] crystal, figure 6.4 shows that the unit cell volume increased gradually during the heating process, with a steeper slope towards the end of the simulation when the temperature reached the 360 K and 400 K lines. This volume increase can be explained by a larger spacing between each molecule in the lattice as a consequence of more rotational freedom for the TMA molecules at higher temperatures. From table 7.1, it is clear that a volume increase is expected when going from the starting configuration Amm2 to the Cmcm phase, however the unit cell volume is expected to decrease upon the further transition to the plastic $Pm\bar{3}m$ mesophase. This high temperature phase is highly disordered due to the rotational freedom of the molecules, and almost all symmetry is broken at this point as this is the final stage before the crystal melts to the liquid phase. A possible explanation why a volume decrease is not seen in figure 6.4 may therefore be that it is hard to measure the unit cell parameters accurately for such a disordered phase. Another possibility is that the temperature in this project wasn't high enough to facilitate the transition to the plastic mesophase, and the final structure after the slow heating process could also be the Cmcm phase. However, figure 6.4 shows that there are two distinct volume increases around 360 K and 400 K, respectively, indicating that the starting configuration Amm2 undergoes two subsequent phase transitions, first to the Cmcm phase and then to the $Pm\bar{3}m$ phase.

This agrees well with the symmetry analysis from the reconstructed lattice parameters in figure 6.8. This figure shows that for lattice parameter a, there are two distinct lattice parameters in the beginning of

the heating process; one at about 6.5 Å and one at about 13.5 Å, where the one at 13.5 Å corresponds to the supercell parameter. The a lattice parameter at 6.5 Å disappears once the high temperature phase is reached, after about 700 ps. This means that no symmetry elements have been found in this phase, confirming that the TMA[$FeCl_4$] crystal undergoes a transition to the plastic $Pm\bar{3}m$ mesophase. Both lattice parameters b and c show a similar disappearance of the lattice parameters around 7 Å upon the transition to the high temperature phase, which is probably due to the extreme rotational disorder of this phase. This agrees well with the XRD spectrum of the TMA[$FeCl_4$] crystal in figure 6.10, as the XRD-lines becomes more blurred out in the high temperature area, indicating a lot of disorder and lack of symmetry.

Figure 6.8 also shows that during the cooling process, the a lattice parameter at about 6.5 Å reappears after about 1000 ps, indicating a re-crystallisation from the high temperature mesophase to a more ordered phase with symmetry. The b lattice parameter at about 7 Å that disappears after about 700 ps reappears at 9 Å after about 1000 ps, and the c lattice parameter at about 7 Å that disappears after about 700 ps doesn't seem to reappear at all during the cooling process. Although this is a very rough method to analyse the crystal symmetry, these results indicate that the TMA[$FeCl_4$] crystal recrystallises to the Cmcm phase during the cooling process, by comparison with table 7.1. The Cmcm phase has a c lattice parameter that is considerably larger than the a and b lattice parameters, and the b lattice parameter is larger than the a lattice parameter, which qualitatively matches well with the crystal data on Cmcm in table 7.1. This hypothesis is also substantiated by the simulated XRD spectrum for the TMA[$FeCl_4$] crystal, where a new XRD line appears at point C in figure 6.10 during the cooling process, indicating that the crystal relaxes to a different structure than the initial Amm2 phase. By comparing figure 6.4 a) and figure 6.5 a), it is also clear that the unit cell volume increases in two steps during the heating process, while the volume decrease during the cooling process happens in one single step. This agrees well with the two phase transitions Amm2 $\rightarrow$ Cmcm $\rightarrow$ $Pm\bar{3}m$ for the heating process, followed by a single phase transition $Pm\bar{3}m \rightarrow$ Cmcm for the cooling process. The absence of a transition back to the original Amm2 phase indicates a lack of thermal hysteresis, which has also been reported for ZrO_2 between the monoclinic and tetragonal phases by using *ab initio* MD simulations with on-the-fly trained machine learned force fields [30].

For the TMA[$FeBr_4$] crystal, figure 6.4 indicates that there might be a phase transition in the beginning of the heating process, as the unit cell volume and lattice parameters changes drastically after only a couple of picoseconds. As the starting configuration Amm2 is a 330 K phase while the heating process starts at 200 K, a possible explanation for this behaviour could be that there is a phase transition to a lower

temperature state, possibly Pma2. According to table 7.1, Pma2 has a smaller unit cell volume, larger lattice parameter a, and smaller lattice parameters b and c compared to the Amm2 phase. This agrees well with the changes observed in figure 6.4, with decreasing unit cell volume, decreasing lattice parameters b and c and increasing lattice parameter a.

The reconstructed lattice parameters for TMA[$FeBr_4$] in figure 6.9 also indicates that there is a phase transition in the beginning of the heating process. Starting with two a lattice parameters at about 7 Å and 14 Å in the beginning of the heating process, there appears a new a lattice parameter at about 6.5 Å after approximately 100 ps. At the same time, there appears a b lattice parameter at about 6.5 Å and a c lattice parameter at about 7 Å. These changes in crystal symmetry may indicate a phase transition to the Pma2 phase. Possible reasons could be that this phase is more energetically favourable for the TMA[$FeBr_4$] crystal at low temperatures, or that the steric hindrance of the TMA molecules results in a relaxation to this phase.

Figure 6.4 shows that there are few significant changes in the lattice parameters for the TMA[$FeBr_4$] crystal after the assumed transition to the Pma2 phase (after about 100 ps). There is a continuous, slight increase in a, b, c and the unit cell volume throughout the rest of the heating process, but this is probably due to more movement within the crystal and larger lattice spacing at higher temperatures. After reaching 400 K there is a final change in lattice parameters with a small increase in a and decrease in b and c that may indicate a new phase transition, possibly back to the initial Amm2 phase or the Cmcm phase. However, these changes are small compared to the initial ones, and they could also be a result of something else.

By comparing the observed changes in lattice parameters in the TMA[$FeBr_4$] crystal with the energy per atom in figure 6.6 after 700 ps, it is clear that the energy decreases drastically after reaching the 400 K line. This is unexpected, as the temperature is still increasing at this point. This behaviour could either indicate that the system reaches a phase transition, that melting of the crystal is about to occur or that there is an error within the machine learned potentials at this point. From the symmetry analysis in figure 6.9 and the XRD spectrum in figure 6.11, it does not seem to be any phase transitions for the TMA[$FeBr_4$] crystal in the high temperature area, indicating that the last of these alternatives could be the case. However, to get a better understanding of this, future work should aim for heating the TMA[$FeBr_4$] crystal to even higher temperatures over longer time periods, and validate the force fields up against pure *ab initio* runs in order to improve their accuracy.

Although the results in this project indicates that the TMA[$FeBr_4$] crystal did not undergo a phase transition to the plastic mesophase, this doesn't mean that such a phase does not exist for the TMA[$FeBr_4$]

crystal. Since Br is below Cl in the periodic table, the ionic radii of Br are larger than those of Cl [36], and the $[FeBr_4]^-$ molecule is therefore larger than the $[FeCl_4]^-$ molecule. This means that the steric hindrance of the TMA molecules in the TMA$[FeBr_4]$ crystal is larger than within the TMA$[FeCl_4]$ crystal, and the TMA molecules can therefore rotate more freely in TMA$[FeCl_4]$ than in TMA$[FeBr_4]$. This also implies that the temperature needed to facilitate the transition to the plastic mesophase probably is lower for the TMA$[FeCl_4]$ crystal than for the TMA$[FeBr_4]$ crystal. In other words, there could exist a mesophase for the TMA$[FeBr_4]$ crystal at higher temperatures than those investigated in this project.

When it comes to the cooling of the TMA$[FeBr_4]$ crystal, figure 6.5 shows few significant changes in the lattice parameters and unit cell volume. However, from figure 6.9 there seems to be a change in symmetry after about 1100 ps, where the a, b and c lattice parameters around 6.5 Å and 7 Å suddenly disappears. This corresponds to a time of approximately 300 ps in figure 6.5, since the heating and cooling processes were run for 800 ps each. A possible explanation for this symmetry change could be that there is a transition to a lower temperature phase, but it could also be that the crystal stays in the Pma2 phase throughout the simulation and the symmetry break in figure 6.9 is a result of something else. Reconstructing the unit cell lattice parameters based on the symmetry of the Fe atoms is a rough way of analysing the crystal structure, and figure 6.5 gives a more accurate picture of how the size of the $2\times2\times2$ supercell changes during the simulation than figure 6.9.

It is important to notice that the variation in both temperature, lattice parameters and unit cell volume in figure 6.4 and 6.5 is big, which can be seen from the broad distribution of dots in the scatter plots. This means that one must be careful drawing conclusions solely based on these plots, as they merely show the average trend over a short amount of time for a small simulation cell. Larger simulation cells and longer simulation times would probably give a better description of a bulk material.

Another important aspect is that the accuracy of the calculations in this project is highly dependent on the quality of the machine learned force fields. In this project, the only validation of the force fields was how accurately they succeeded in predicting the material properties seen in experiments, but ideally it would have been better with a more thorough validation of the force fields in advance of the production calculations predicting the phase transitions.

7.1.2 *Simulated XRD spectra*

The XRD spectra for the two plastic crystals provides another way of analysing the changes in crystal structure and identify possible phase

transitions. In figure 7.1, which is retrieved from Walker *et al* [35], the XRD spectrum for the plastic crystal TMA[$FeBrCl_3$] is presented. In their work, Walker *et al* obtained this plot by heating the crystals up to 200 °C with a heating rate of 0.2 °C/s, holding this temperature for 30 minutes before cooling the crystals down to room temperature again with a cooling rate of 0.4 °C/s [35]. The maximum temperature of 200 °C corresponds to 473 K, which is higher than the maximum temperature used in this project. Also, the plastic crystal TMA[$FeBrCl_3$] is not exactly the same as those investigated in this project, however it has the same crystal structure and is a good reference for comparing the XRD spectra of TMA[$FeCl_4$] and TMA[$FeBr_4$]. However, it is important to notice that Walker *et al* investigated the long-range crystallographic structure of the TMA[$FeBrCl_3$] compound, while in this thesis the plastic crystals were studied by using a relatively small supercell. The local structure of these 2×2×2 simulation cells was used to project the long-range structure of the plastic crystals, but will not have the true long-range behaviour of a bulk material as periodic boundary conditions makes every mirror image of the simulation cell look exactly the same.

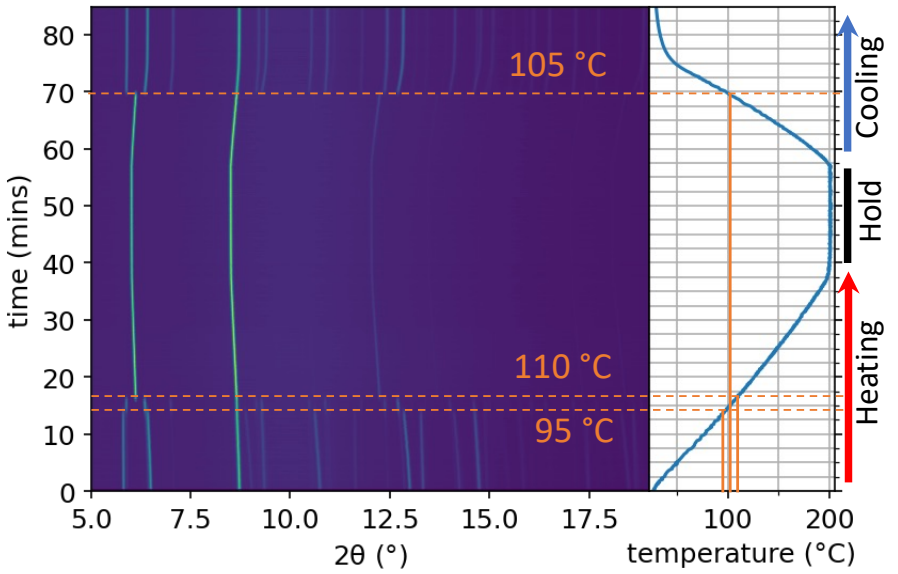

Figure 7.1: XRD spectrum for the plastic crystal TMA[$FeBrCl_3$], retrieved with permission from Walker [35].

For the TMA[$FeCl_4$] crystal, the XRD spectrum in figure 6.10 clearly shows a splitting of spectral lines around 6.3° 2θ that merges into one single line at point A upon the transition to the high temperature mesophase. This agrees well with the findings presented in figure 7.1, where the same splitting and merging tendency can be observed around 6° 2θ. However, the gap between the lines in figure 7.1 is larger than in figure 6.10, which might be due to the presence of a Br atom in the TMA[$FeBrCl_3$] crystal. Figure 6.10 also shows that there is

a slight bending of spectral lines towards lower 2θ values in the high temperature area, which agrees well with the bending tendency seen in figure 7.1. At point B in figure 6.10 there is a re-spitting of lines indicating that the structure recrystallises to the Cmcm phase after about 1050 ps. This agrees well with the splitting of lines in figure 7.1, although the in situ XRD experiments were performed over a much longer time frame. The appearance of a new spectral line at point C in figure 6.10 can also be observed in figure 7.1 around 7.5° 2θ, although this line seems to appear at slightly lower 2θ values in the case of TMA[$FeBrCl_3$] compared to the TMA[$FeCl_4$] crystal studied in this project. This might be due to the differences in composition for the two crystals. The spectral line around 9° 2θ (point D) in figure 6.10 can also be found in the figure 7.1, but again the XRD line in the TMA[$FeBrCl_3$] spectrum appears to be shifted towards lower 2θ values compared to TMA[$FeCl_4$].

As discussed in the previous section, these results confirms that there probably is a transition from the Amm2 phase to the plastic mesophase via the Cmcm phase in the TMA[$FeCl_4$] crystal during the heating process from 200 K to 400 K. The emergence of a new spectral line during the cooling process suggests that recrystallization from the plastic mesophase led to a different space group than the initial Amm2 phase, most likely the Cmcm phase. This agrees well with the findings from the analysis of the lattice parameters for the TMA[$FeCl_4$] crystal.

For the TMA[$FeBr_4$] crystal, figure 6.11 shows a similar splitting of spectral lines around 6.3° 2θ (point A) as observed in the TMA[$FeCl_4$] crystal. The reason for the broader splitting in TMA[$FeBr_4$] compared to TMA[$FeCl_4$] may be contextualized by considering the broader splitting in TMA[$FeBrCl_3$] relative to TMA[$FeCl_4$]. The crystals containing Br have a wider splitting of spectral lines compared to TMA[$FeCl_4$], indicating that the presence of Br contributes to a broadening of spectral line splitting in addition to inducing a downward shift in the position of the spectral lines towards lower 2θ values. Also, figure 6.11 shows that the two lines doesn't merge together in the high temperature area, indicating that there is no transition to the plastic mesophase in the case of TMA[$FeBr_4$]. This agrees well with the observed trend in lattice parameters for TMA[$FeBr_4$] in figure 6.4 and 6.5. As mentioned, the reason for this absence of a transition to the plastic mesophase could be due to hindered rotation of the TMA molecules due to larger inorganic anions compared to TMA[$FeCl_4$]. For future work, it would be interesting to investigate even higher temperatures to see how much energy is required in order for the TMA[$FeBr_4$] crystal to enter the plastic mesophase, and how close to the melting temperature this transition finds place.

7.2 ROTATIONAL DYNAMICS

Figure 6.12 shows the rotational autocorrelation function for the two plastic crystals with a lag value of 100. For the TMA[$FeCl_4$] crystal, there is a higher degree of correlation between the TMA molecules within the relevant time frame at 200 K than at 300 K and 400 K. In other words, the angle of the tracked methyl group relative to its starting configuration increases with increasing temperature and increasing degrees of freedom. This is as expected, because higher temperatures are associated with more rotational freedom and less correlation between subsequent simulation steps. The 300 K curve is slightly below the 400 K curve, indicating that there is more rotational freedom within the 300 K phase than within the 400 K phase. This agrees well with the trajectory plots of the tracked methyl groups in figure 6.13. The reason why the 300 K and 400 K phases in the TMA[$FeCl_4$] crystal appears to have approximately the same amount of rotational freedom might be that there is less steric hindrance for TMA[$FeCl_4$] compared to TMA[FeBr], meaning that there is less energy required in order to make the TMA molecules rotate freely. If the TMA molecules can rotate freely in the 300 K phase, it is reasonable that the extra energy in the 400 K phase won't contribute with much more rotational freedom, resulting in almost the same degree of correlation between simulation steps at 300 K and 400 K.

For the TMA[$FeBr_4$] crystal, figure 6.12 shows that there is a clear relationship between decreasing autocorrelation within the structure and increasing temperature. This agrees well with figure 6.14, where the trajectories of the tracked methyl groups occupy more space and become more disordered with increasing temperature. Figure 6.12 also shows that the rotational autocorrelation is larger for the TMA[$FeBr_4$] crystal than for the TMA[$FeCl_4$] crystal within a time frame of 100 ps, by pairwise comparing the 200 K, 300 K and 400 K curves. This is probably due to the steric hindrance of the TMA molecules in the TMA[$FeBr_4$] compound, restricting the rotations and therefore increasing the correlation between subsequent steps.

It is important to remember that although the motion of the TMA molecules have been discussed extensively in the previous sections, both the inorganic anions and the organic cations play an important role in determining the properties of the plastic crystals studied in this project. For both these molecules, the size and the composition can be changed in order to engineer new materials, making plastic crystals a versatile class of materials with a wide range of possible applications. The results presented in the current work indicates that the Curie temperature, T_C, of the TMA[$FeCl_4$] crystal is lower than the Curie temperature of the TMA[$FeBr_4$] crystal, as the transition from the crystalline phase to the plastic mesophase found place at lower temperatures for the TMA[$FeCl_4$] crystal than for the

TMA[$FeBr_4$] crystal (although no transition to this mesophase was observed for TMA[$FeBr_4$] in this project). This is as expected since the steric hindrance of the TMA cations within the TMA[$FeBr_4$] crystal is larger than within the TMA[$FeCl_4$] crystal, due to Br being larger than Cl. Changing the organic cation to e.g. tetraethylammonium (TEA) would have increased the steric hindrance even further, and with that the Curie temperature would probably have been increased even more. In addition to affecting the rotational freedom of the organic cations, the inorganic anions also plays an important role when it comes to the electronic properties of these crystals, and changing the composition of the anion will affect e.g. the dielectric and piezoelectric coefficients of the crystal. In previous work, it has been shown that e.g. the TMA[$FeCl_4$] crystal have a larger band gap and smaller dielectric constant than the TMA[$FeBr_4$] crystal, as the electronic orbitals of Br overlap more than in Cl, and the valence electrons of Br are more loosely bound to the nucleus than in Cl due to Br being below Cl in the periodic table [2].

7.3 FURTHER WORK

In this project, the phase transitions and rotational dynamics of the plastic crystals TMA[$FeCl_4$] and TMA[$FeBr_4$] were investigated. Although the methods presented here gave a good pictures of how these materials work on a microscopic level, there are several ways to extend and improve the project.

First of all, a natural continuation of this project would be to simulate other low temperature plastic crystals using the same methods as presented here, playing around with the composition of the structures without introducing foreign elements. The organic tetramethylammonium (TMA) cation could be replaced by e.g. tetraethylammonium (TEA), and the inorganic anions [$FeCl_4$] and [$FeBr_4$] could be replaced by [$FeBrCl_3$] or other combinations of Br and Cl.

Secondly, the plastic crystals investigated in this thesis could be heated to even higher temperatures to see how much energy is required in order for the TMA[$FeBr_4$] compound to enter the plastic mesophase. Also, a slower heating and cooling rate could be used in order to make the simulation conditions closer to those of real experiments.

Another important aspect is validating the machine learning force fields and making them more accurate. In this project, they were only generated for a single starting configuration of the two plastic crystals, so in order to increase their accuracy one could have trained them on different crystal configurations and validated them towards pure *ab initio* molecular dynamics runs. In previous work, 19 different starting configurations of the TMA[$FeCl_4$] and TMA[$FeBr_4$] crystals were investigated, corresponding to the 19 unique rotations of

the TMA molecules in the x-, y- and z-directions within a unit cell [2]. These could have been used as starting points to train the force fields on a wider range of molecular configurations.

Lastly, one could have investigated other functionals than the PBEsol + U functional for the DFT calculations. In previous studies of plastic crystals such as $HQReO_4$ and $LiNbO_3$, van der Waals (vdW) density functionals have been used to model and study the dielectric, piezoelectric and elastic properties of these materials [14]. As a continuation of this project, one could therefore have predicted the phase transitions using the vdW functionals and compared the results with those from the PBEsol + U functional.

8

CONCLUSION

The aim of this project was to predict the phase transitions and study the rotational dynamics in the plastic crystals TMA[$FeCl_4$] and TMA[$FeBr_4$] by using *ab initio* molecular dynamics simulations with machine learned force fields. This was achieved by investigating the change in lattice parameters, unit cell volume and XRD spectra for the two compounds upon heating and cooling from 200 K to 400 K and back again, in addition to analysing the autocorrelation within each structure at 200 K, 300 K and 400 K.

For TMA[$FeCl_4$], the results indicated that there was a phase transition from the initial Amm2 phase to the plastic mesophase via the Cmcm phase during the heating process, and then a transition back to the Cmcm phase during the cooling process. For TMA[$FeBr_4$] on the other hand, the results indicated that the crystal structure relaxed from the initial Amm2 phase to the lower temperature Pma2 phase in the beginning of the heating process, and didn't seem to reach the plastic mesophase at all. This is likely due to steric hindrance of the TMA molecules in TMA[$FeBr_4$], as the inorganic anion $[FeBr_4]^-$ is larger than $[FeCl_4]^-$ since Br is below Cl in the periodic table. This indicates that more energy is required to get full rotational freedom in the TMA[$FeBr_4$] crystal, and the plastic mesophase could exist at higher temperatures than those investigated in this project. This agrees well with the results from the investigation of the rotational dynamics, where the autocorrelation analysis showed that there was more rotational freedom in the TMA[$FeCl_4$] crystal than in the TMA[$FeBr_4$] crystal, and that the rotational freedom increased with increasing temperature for both crystals.

As a continuation of this project, one could have investigated other plastic crystals with the same composition and structure, such as TEA[$FeCl_4$], TEA[$FeBr_4$] or TMA[$FeBrCl_3$]. It is also necessary to investigate the TMA[$FeBr_4$] crystal over wider temperature ranges and longer time periods, in order to get a better understanding of the rotational dynamics and phase transitions within this crystal on a microscopic level. Finally, investigating different functionals such as the van der Waals functionals would provide an interesting comparison for the PBEsol + U functional. This would give a deeper understanding of how different approaches to the first principles calculations affects the predicted crystal properties.

BIBLIOGRAPHY

[1] J. Timmermans. «Plastic crystals: a historical review.» In: *J. Phys. Chem. Solids* 18.1 (1961), pp. 1–8.

[2] S. Meltzer. *First Principles Characterisation of the Structural and Electronic Properties of Plastic Crystals: [FeCl4][(CH3)4N] and [FeBr4][(CH3)4N]*. Project report in TMT4510. Department of Materials Science & Engineering, NTNU, Dec. 2022.

[3] J. Valasek. «Piezo-Electric and Allied Phenomena in Rochelle Salt.» In: *Physical Review* 17.4 (Apr. 1921), pp. 475–481. ISSN: 0031-899X. DOI: 10.1103/PhysRev.17.475.

[4] J. Briscoe and S. Dunn. *Nanostructured Piezoelectric Energy Harvesters*. Springer, 2014, pp. 3–9. URL: www.doi.org/10.1007/978-3-319-09632-2.

[5] S. Mukherjee, D. Phuyal, C. U. Segre, S. Das, O. Karis, T. Edvinsson, and H. Rensmo. «Structure and Electronic Effects from Mn and Nb Co-doping for Low Band Gap BaTiO3 Ferroelectrics.» In: *The Journal of Physical Chemistry C* 125.27 (July 2021), pp. 14910–14923. ISSN: 1932-7447. DOI: 10.1021/acs.jpcc.1c02539.

[6] Y. Wang, J. Yan, H. Cheng, N. Chen, P. Yan, F. Yang, and J. Ouyang. «Lead zirconate titanate and barium titanate bi-layer ferroelectric films on Si.» In: *Ceramics International* 45.7 (May 2019), pp. 9032–9037. ISSN: 02728842. DOI: 10.1016/j.ceramint.2019.01.237.

[7] T. Takenaka. «Piezoelectric properties of some lead-free ferroelectric ceramics.» In: *Ferroelectrics* 230.1 (May 1999), pp. 87–98. ISSN: 0015-0193. DOI: 10.1080/00150199908214902.

[8] X. Feng, B. D. Yang, Y. Liu, Y. Wang, C. Dagdeviren, Z. Liu, A. Carlson, J. Li, Y. Huang, and J. A. Rogers. «Stretchable Ferroelectric Nanoribbons with Wavy Configurations on Elastomeric Substrates.» In: *ACS Nano* 5.4 (Apr. 2011), pp. 3326–3332. ISSN: 1936-0851. DOI: 10.1021/nn200477q.

[9] A. H. King. «Our elemental footprint.» In: *Nature Materials* 18.5 (May 2019), pp. 408–409. ISSN: 1476-1122. DOI: 10.1038/s41563-019-0334-3.

[10] M. Yoneya and J. Harada. «Molecular Dynamics Simulation Study of the Plastic/Ferroelectric Crystal Quinuclidinium Perrhenate.» In: *The Journal of Physical Chemistry C* 124.3 (Jan. 2020), pp. 2171–2177. ISSN: 1932-7447. DOI: 10.1021/acs.jpcc.9b09559. URL: https://pubs.acs.org/doi/pdf/10.1021/acs.jpcc.9b09559.

[11] K. Yang, Z. Liao, Z. Zhang, L. Yang, and S. Hirano. «Ionic plastic crystal-polymeric ionic liquid solid-state electrolytes with high ionic conductivity for lithium ion batteries.» In: *Materials Letters* 236 (Feb. 2019), pp. 554–557. ISSN: 0167577X. DOI: 10.1016/j.matlet.2018.11.003.

[12] D. Reuter, K. Seitz, P. Lunkenheimer, and A. Loidl. «Ionic conductivity and relaxation dynamics in plastic crystals with nearly globular molecules.» In: *The Journal of Chemical Physics* 153.1 (July 2020), p. 014502. ISSN: 0021-9606. DOI: 10.1063/5.0012430.

[13] R. J. D. Tilley. *Understanding Solids*. 2nd ed. Wiley, 2013.

[14] E. D. Sødahl, J. Walker, and K. Berland. «Piezoelectric Response of Plastic Ionic Molecular Crystals: Role of Molecular Rotation.» In: *Crystal Growth & Design* 23.2 (Feb. 2023), pp. 729–740. ISSN: 1528-7483. DOI: 10.1021/acs.cgd.2c00854.

[15] J. Harada. «Plastic/ferroelectric molecular crystals: Ferroelectric performance in bulk polycrystalline forms.» In: *APL Materials* 9.2 (Feb. 2021), p. 020901. ISSN: 2166-532X. DOI: 10.1063/5.0039066.

[16] G. J. Kabo, A. V. Blokhin, M. B. Charapennikau, A. G. Kabo, and V. M. Sevruk. «Thermodynamic properties of adamantane and the energy states of molecules in plastic crystals for some cage hydrocarbons.» In: *Thermochimica Acta* 345.2 (Mar. 2000), pp. 125–133. ISSN: 00406031. DOI: 10.1016/S0040-6031(99)00393-7.

[17] J. Lee, W. Seol, G. Anoop, S. Samanta, S. Unithrattil, D. Ahn, W. Kim, G. Jung, and J. Jo. «Stabilization of Ferroelectric Phase in Highly Oriented Quinuclidinium Perrhenate (HQReO4) Thin Films.» In: *Materials* 14.9 (Apr. 2021), p. 2126. ISSN: 1996-1944. DOI: 10.3390/ma14092126.

[18] J. Timmermans. «Researches in stoichiometry. 1. heat of fusion of organic compounds.» In: *Bull. Soc. Chim. Belg* 44 (1935), pp. 17–40.

[19] H. Sun, X. Zhang, M. Zhang, J. Lv, L. Wang, and W. Huang. «High-Performance organic lithium-ion battery with plastic crystal electrolyte.» In: *Organic Electronics* 87 (2020).

[20] J. Harada, N. Yoneyama, S. Yokokura, Y. Takahashi, A. Miura, N. Kitamura, and T. Inabe. «Ferroelectricity and Piezoelectricity in Free-Standing Polycrystalline Films of Plastic Crystals.» In: *J. Am. Chem. Soc* 140 (2018), p. 2022. DOI: 10.1021/jacs.7b10539.

[21] D. S. Sholl and J. A. Steckel. *Density Functional Theory - A Practical Introduction*. Wiley, 2009.

[22] G. Kresse and J. Hafner. «Ab initio molecular dynamics for liquid metals.» In: *Physical Review B* 47.1 (Jan. 1993), pp. 558–561. ISSN: 0163-1829. DOI: 10.1103/PhysRevB.47.558.

[23] G. Kresse and J. Furthmüller. «Efficiency of ab-initio total energy calculations for metals and semiconductors using a plane-wave basis set.» In: *Computational Materials Science* 6.1 (July 1996), pp. 15–50. ISSN: 09270256. DOI: 10.1016/0927-0256(96)00008-0.

[24] G. Kresse and J. Furthmüller. «Efficient iterative schemes for ab initio total-energy calculations using a plane-wave basis set.» In: *Physical Review B* 54.16 (Oct. 1996), pp. 11169–11186. ISSN: 0163-1829. DOI: 10.1103/PhysRevB.54.11169.

[25] J. G. Lee. *Computational Materials Science – an introduction*. CRC Press, 2015.

[26] VASP. *Langevin thermostat*. Apr. 2022. URL: https://www.vasp.at/wiki/index.php/Langevin_thermostat.

[27] VASP. *Nose-Hoover thermostat*. Apr. 2022. URL: https://www.vasp.at/wiki/index.php/Nose-Hoover_thermostat.

[28] IBM. *What is machine learning?* URL: https://www.ibm.com/topics/machine-learning?mhsrc=ibmsearch_a&mhq=machine%20learning.

[29] I. Goodfellow, Y. Bengio, and A. Courville. *Deep Learning*. MIT Press, 2016.

[30] C. Verdi, F. Karsai, P. Liu, R. Jinnouchi, and G. Kresse. «Thermal transport and phase transitions of zirconia by on-the-fly machine-learned interatomic potentials.» In: *npj Computational Materials 2021 7:1* 7.1 (Sept. 2021), pp. 1–9. ISSN: 2057-3960. DOI: 10.1038/s41524-021-00630-5.

[31] VASP. *Part 2: Machine learning force fields*. URL: https://www.vasp.at/tutorials/latest/md/part2.

[32] VASP. *Machine learning force field: Theory*. 2023. URL: https://www.vasp.at/wiki/index.php/Machine_learning_force_field:_Theory.

[33] K. Momma and F. Izumi. «VESTA3 for three-dimensional visualization of crystal, volumetric and morphology data.» In: *Journal of Applied Crystallography* 44.6 (Dec. 2011), pp. 1272–1276. DOI: 10.1107/S0021889811038970.

[34] S. P. Ong, W. D. Richards, A. Jain, G. Hautier, M. Kocher, S. Cholia, D. Gunter, V. L. Chevrier, K. A. Persson, and G. Ceder. «Python Materials Genomics (pymatgen): A robust, open-source python library for materials analysis.» In: *Computational Materials Science* 68 (Feb. 2013), pp. 314–319. ISSN: 09270256. DOI: 10.1016/j.commatsci.2012.10.028.

[35] J. Walker, K. P. Marshall, J. Salgado-Beceiro, B. A. D. Williamson, N. S. Løndal, S. Castro-Garcia, M. S. Andújar, S. M. Selbach, D. Chernyshov, and M. Einarsrud. «Mesophase Transitions in [(C2H5)4 N][FeBrCl3] and [(CH3)4 N][FeBrCl3] Ferroic Plastic Crystals.» In: *Chemistry of Materials* 34.6 (Mar. 2022), pp. 2585–2598. ISSN: 0897-4756. DOI: 10.1021/acs.chemmater.1c03778.

[36] R. D. Shannon. «Revised Effective Ionic Radii and Systematic Studies of Interatomic Distances in Halides and Chalcogenides.» In: *Acta Cryst.* A32 (1976), pp. 751–767.

A

VASP INCAR FILES

This section provides an overview of the different INCAR files used for the VASP calculations in this project.

A.1 GENERATION OF MLFF

Listing A.1 contains the INCAR tags used for the generation of the MLFFs with the Langevin thermostat. The parameters TEBEG and TEEND gives the starting and final temperature for the simulation, respectively. The force fields were created by running simulations first from 200 K to 200 K, then from 200 K to 400 K and finally from 400 K to 400 K, where the only INCAR changes between these three calculations were the TEBEG and TEEND parameters. The file presented below gives the tags for the 200 K to 200 K calculation. By changing the TEBEG and TEEND parameters, the INCAR could be used for other two calculations.

Listing A.1: INCAR parameters for the generation of MLFFs with the Langevin thermostat at 200 K.

```
SYSTEM = Generic Input

! start Parameters
NWRITE     = 2      ! Medium-level information output
ISTART     = 1      ! read existing wavefunction; if there
INIWAV     = 1      ! Random initial wavefunction; otherwise

! parallelisation
NCORE = 16          ! No. cores per orbital

! electronic relaxation
PREC    = Low       ! Precision level
ALGO    = Fast      ! SCF minimisation algorithm; 38/48 combo
ENMAX   = 500       ! Plane-wave cutoff
NELM    = 1000      ! Max SCF steps
NELMIN  = 2         ! Min SCF steps
EDIFF   = 1E-06     ! SCF energy convergence
GGA     = PS        ! PBEsol exchange-correlation
LASPH   = .TRUE.    ! Non-spherical elements; d/f convergence
LREAL   = Auto      ! Projection operators: automatic

! ionic relaxation
EDIFFG = -0.01      ! Ionic convergence; eV/AA^3
NSW    = 20000      ! Max ionic steps
```

```
IBRION = 0          ! Algorithm: 0-MD; 1-Quasi -New; 2-CG
ISIF   = 3          ! Stress/relaxation:2-Ions;3-Shape/Ions/V
ISYM   = 0          ! Symmetry: 0-none; 2=GGA; 3=hybrids
NBLOCK = 1          ! Update XDATCAR every X steps
ISMEAR = -1         ! Gaussian smearing; metals:1
SIGMA  = 0.0258     ! Smearing value in eV; metals:0.2
IWAVPR = 1          ! charge density extrapolation: 0-non 1-
    charg 2-wave 3-comb
POTIM  = 2          ! Timestep in fs

! molecular dynamics
LWAVE  = F
LCHARG = F
LREAL  = Auto
MDALGO = 3                    ! Langevin thermostat
LANGEVIN_GAMMA   = 0 5 0 0 0  ! friction
LANGEVIN_GAMMA_L = 5          ! lattice friction
PMASS  = 10                   ! lattice mass
TEBEG  = 200                  ! start temp
TEEND  = 200                  ! end temp

! machine learning
ML_LMLFF  = T
ML_ISTART = 0
ML_WTSIF  = 2
ML_LBASIS_DISCARD = .TRUE.
RANDOM_SEED =   688344966  0   0

! dft+u
LDAU    = .TRUE.                ! Activate DFT+U
LDATYPE = 2                     ! Dudarev; only U-J matters
LDAUL   = 2 -1 -1 -1 -1         ! Orbitals for each species
LDAUU   = 5.5 0 0 0 0           ! U for each species
LDAUJ   = 0  0 0 0 0            ! J for each species
LMAXMIX = 4                     ! Mixing cut-off; 4-d, 6-f
```

A.2 PHASE TRANSITION CALCULATIONS

Listing A.2 gives the `INCAR` parameters for the slow heating process from 200 K to 400 K for the two plastic crystals. For the cooling process, the `TEBEG` and `TEEND` parameters were changed to 400 and 100, respectively.

Listing A.2: INCAR parameters for the slow heating of the plastic crystals from 200 K to 400 K.

```
SYSTEM = Generic Input

! start Parameters
NWRITE     = 2      ! Medium-level information output
```

```
ISTART     = 1      ! read existing wavefunction; if there
INIWAV     = 1      ! Random initial wavefunction; otherwise

! parallelisation
NCORE = 16          ! No. cores per orbital

! electronic relaxation
PREC    = Normal    ! Precision level
ALGO    = Fast      ! SCF minimisation algorithm; 38/48 combo
ENMAX = 500
NELM    = 1000      ! Max SCF steps
NELMIN  = 2         ! Min SCF steps
EDIFF   = 1E-06     ! SCF energy convergence
GGA     = PS        ! PBEsol exchange-correlation
LASPH   = .TRUE.    ! Non-spherical elements; d/f convergence
LREAL   = Auto      ! Projection operators: automatic

! ionic relaxation
EDIFFG = -0.01      ! Ionic convergence; eV/AA^3
NSW = 400000
IBRION = 0
ISIF = 3
ISYM   = 0          ! Symmetry: 0-none; 2=GGA; 3=hybrids
NBLOCK = 50         ! Update XDATCAR every X steps
ISMEAR = -1         ! Gaussian smearing; metals:1
SIGMA  = 0.0258     ! Smearing value in eV; metals:0.2
IWAVPR = 1          ! charge density extrapolation: 0-non 1-
    charg 2-wave 3-comb
POTIM  = 2          ! Timestep in fs

! molecular dynamics
LWAVE  = F
LCHARG = F
LREAL  = Auto
MDALGO = 3                   ! Langevin thermostat
LANGEVIN_GAMMA   = 0 5 0 0 0 ! friction
LANGEVIN_GAMMA_L = 5         ! lattice friction
PMASS  = 200                 ! lattice mass
TEBEG  = 200                 ! start temp
TEEND = 400                  ! end temp

! machine learning
ML_LMLFF  = T
ML_ISTART = 2
ML_WTSIF  = 2
ML_LBASIS_DISCARD = .TRUE.
RANDOM_SEED =   688344966  0   0

! dft+u
LDAU    = .TRUE.                ! Activate DFT+U
LDATYPE = 2                     ! Dudarev; only U-J matters
LDAUL   = 2 -1 -1 -1 -1         ! Orbitals for each species
```

```
LDAUU   = 5.5 0 0 0 0           ! U for each species
LDAUJ   = 0  0 0 0 0            ! J for each species
LMAXMIX = 4                     ! Mixing cut-off; 4-d, 6-f
```

A.3 ROTATIONAL DYNAMICS CALCULATIONS

Listing A.3 gives the INCAR parameters for the constant volume calculations using the Nosé-Hoover thermostat at 200 K. For the analysis of the rotational dynamics at 300 K and 400 K, the TEBEG and TEEND tags were changed accordingly.

Listing A.3: INCAR parameters for the constant volume calculations using the Nosé-Hoover thermostat from 200 K to 200 K.

```
SYSTEM = Generic Input

! start Parameters
NWRITE     = 2      ! Medium-level information output
ISTART     = 1      ! read existing wavefunction; if there
INIWAV     = 1      ! Random initial wavefunction; otherwise

! parallelisation
NCORE = 16          ! No. cores per orbital

! electronic relaxation
PREC    = Normal    ! Precision level
ALGO    = Fast      ! SCF minimisation algorithm; 38/48 combo
ENMAX = 500
NELM    = 1000      ! Max SCF steps
NELMIN  = 2         ! Min SCF steps
EDIFF   = 1E-06     ! SCF energy convergence
GGA     = PS        ! PBEsol exchange-correlation
LASPH   = .TRUE.    ! Non-spherical elements; d/f convergence
LREAL   = Auto      ! Projection operators: automatic

! ionic relaxation
EDIFFG = -0.01      ! Ionic convergence; eV/AA^3
NSW = 50000
IBRION = 0
ISIF = 2
ISYM   = 0          ! Symmetry: 0-none; 2=GGA; 3=hybrids
NBLOCK = 10         ! Update XDATCAR every X steps
ISMEAR = -1         ! Gaussian smearing; metals:1
SIGMA  = 0.0258     ! Smearing value in eV; metals:0.2
IWAVPR = 1          ! charge density extrapolation: 0-non 1-
    charg 2-wave 3-comb
POTIM  = 2          ! Timestep in fs

! molecular dynamics
LWAVE  = F
```

```
LCHARG = F
LREAL  = Auto
MDALGO = 2                    ! Nose-Hoover thermostat
LANGEVIN_GAMMA   = 0 5 0 0 0 ! friction
LANGEVIN_GAMMA_L = 5          ! lattice friction
PMASS  = 200                  ! lattice mass
SMASS  = 0
TEBEG  = 200                  ! start temp
TEEND = 200                   ! end temp

! machine learning
ML_LMLFF  = T
ML_ISTART = 2
ML_WTSIF  = 2
ML_LBASIS_DISCARD = .TRUE.
RANDOM_SEED =   688344966  0   0

! dft+u
LDAU    = .TRUE.                 ! Activate DFT+U
LDATYPE = 2                      ! Dudarev; only U-J matters
LDAUL   = 2 -1 -1 -1 -1          ! Orbitals for each species
LDAUU   = 5.5 0 0 0 0            ! U for each species
LDAUJ   = 0  0 0 0 0             ! J for each species
LMAXMIX = 4                      ! Mixing cut-off; 4-d, 6-f
```

B

ROTATIONAL AUTOCORRELATION FUNCTION

This section presents the plots of the autocorrelation function for the two plastic crystals TMA[$FeCl_4$] and TMA[$FeBr_4$] at 200 K, 300 K and 400 K by using four different lag values; 50, 100, 150 and 200. For the rotational dynamics analysis, a lag value of 100 was chosen as this was the highest one where the plot didn't get inside the cone representing the 95% confidence level.

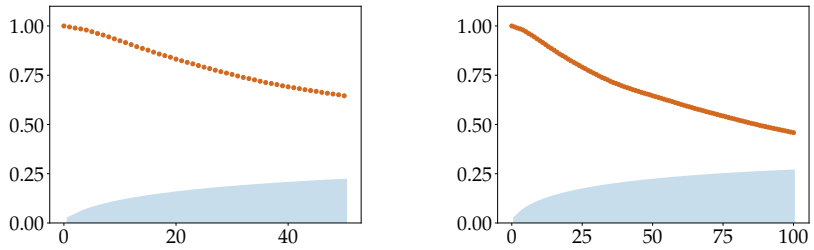

(a) lag = 50

(b) lag = 100

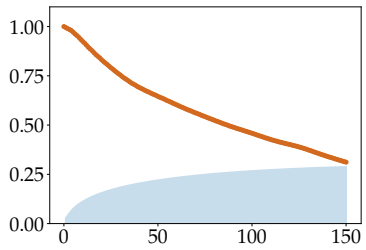

(c) lag = 150

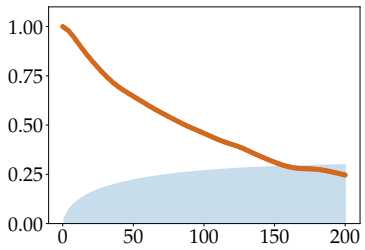

(d) lag = 200

Figure B.1: Autocorrelation for the TMA[$FeCl_4$] crystal at 200 K with lags of a) 50, b) 100, c) 150 and d) 200.

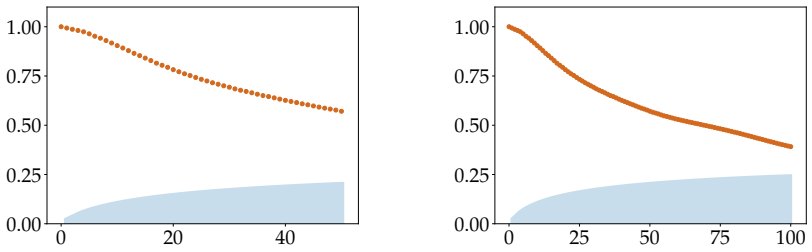

(a) lag = 50 (b) lag = 100

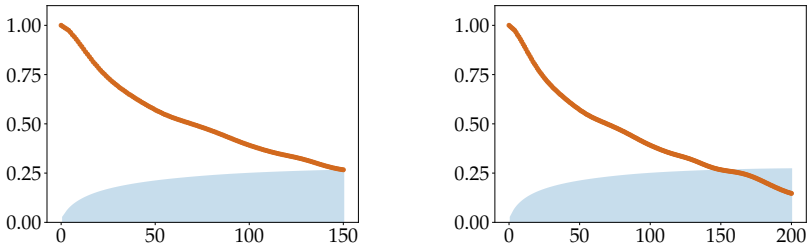

(c) lag = 150 (d) lag = 200

Figure B.2: Autocorrelation for the TMA[$FeCl_4$] crystal at 300 K with lags of a) 50, b) 100, c) 150 and d) 200.

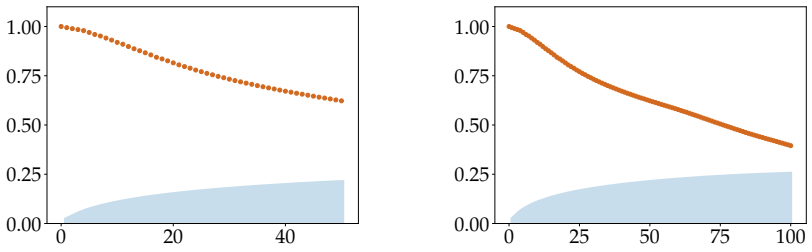

(a) lag = 50 (b) lag = 100

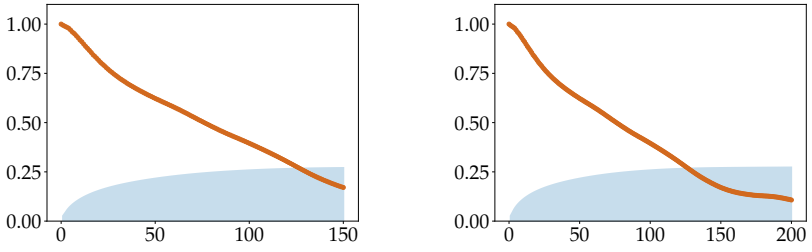

(c) lag = 150 (d) lag = 200

Figure B.3: Autocorrelation for the TMA[$FeCl_4$] crystal at 400 K with lags of a) 50, b) 100, c) 150 and d) 200.

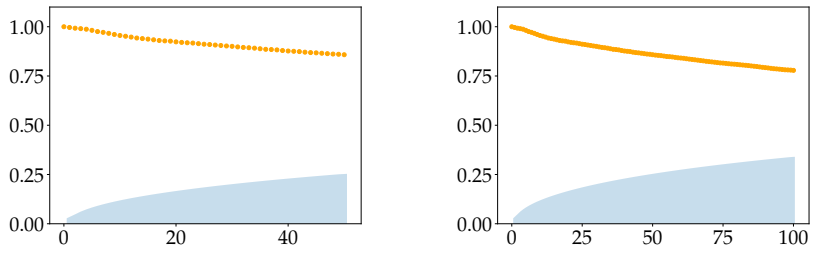

(a) lag = 50 (b) lag = 100

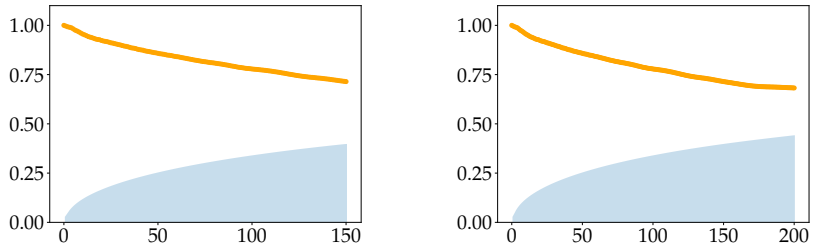

(c) lag = 150 (d) lag = 200

Figure B.4: Autocorrelation for the TMA[$FeBr_4$] crystal at 200 K with lags of a) 50, b) 100, c) 150 and d) 200.

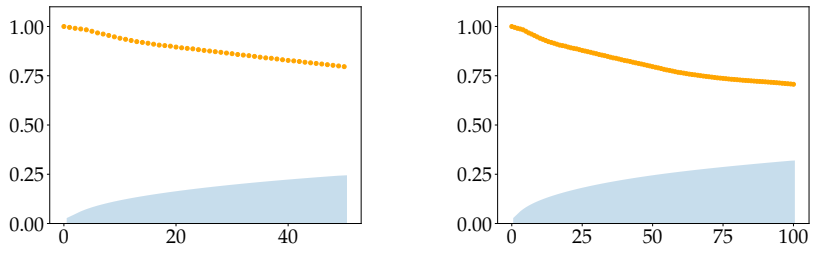

(a) lag = 50 (b) lag = 100

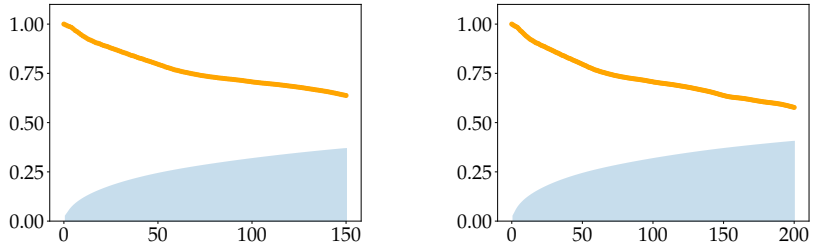

(c) lag = 150 (d) lag = 200

Figure B.5: Autocorrelation for the TMA[$FeBr_4$] crystal at 300 K with lags of a) 50, b) 100, c) 150 and d) 200.

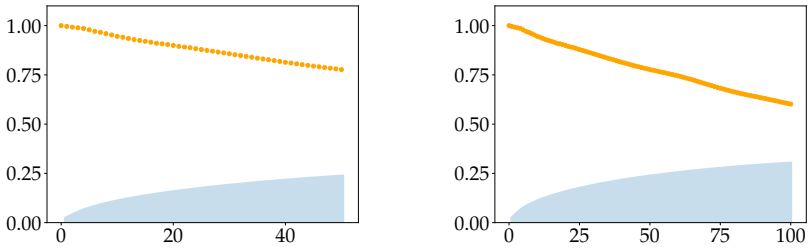

(a) lag = 50 (b) lag = 100

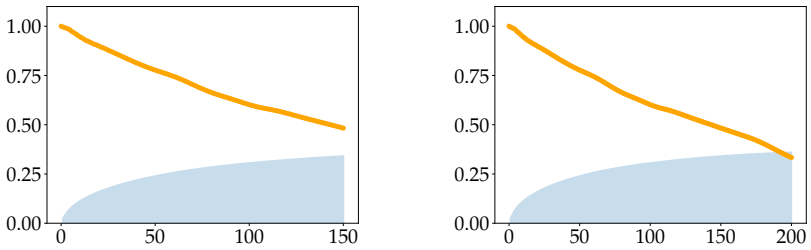

(c) lag = 150 (d) lag = 200

Figure B.6: Autocorrelation for the TMA[$FeBr_4$] crystal at 400 K with lags of a) 50, b) 100, c) 150 and d) 200.

C

CONVERGENCE OF THE CUTOFF ENERGY

Figure C.1 shows the results from the convergence tests of the cutoff energy for the TMA[$FeCl_4$] crystal. This plot is retrieved from previous project work [2]. The convergence test was performed on a TMA[$FeCl_4$] unit cell with a convergence criterion of $< 1\,\text{meV}$. The cutoff energy was only tested on the TMA[$FeCl_4$] crystal because it mainly depends on the carbon and nitrogen atoms, and it is therefore reasonable to assume that changing a Cl atom with a Br atom (in the case of TMA[$FeBr_4$]) would have little effect on the energy cutoff. In this project, a cutoff energy of 500 eV was used for both plastic crystals.

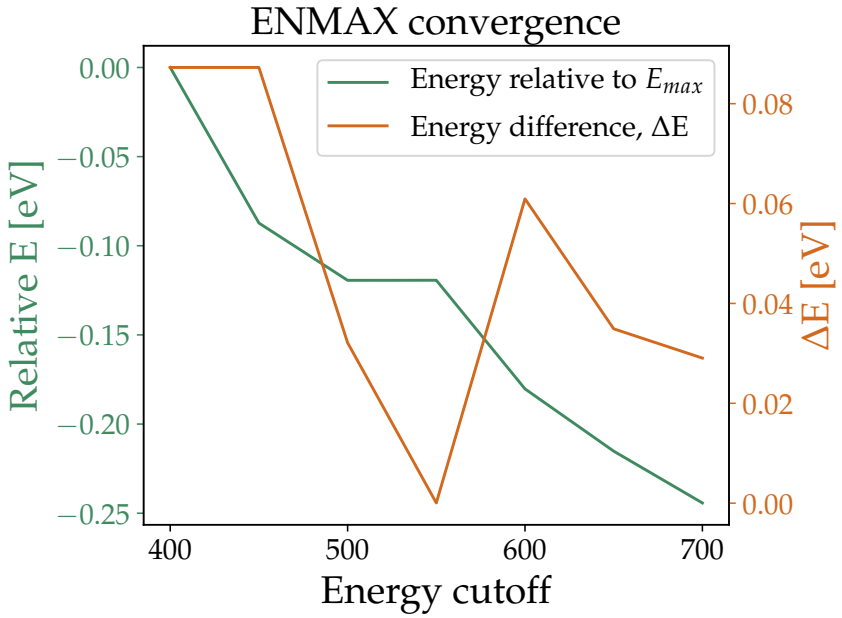

Figure C.1: Convergence test of the cutoff energy for the TMA[$FeCl_4$] crystal. Figure retrieved from [2].

D

BEEF PLOTS FOR THE MLFF GENERATION

In figure D.1 and D.2, the Bayesian error estimate of forces (BEEF) for the generation of the machine learned force fields from 200 K to 200 K and from 400 K to 400 K are presented, respectively.

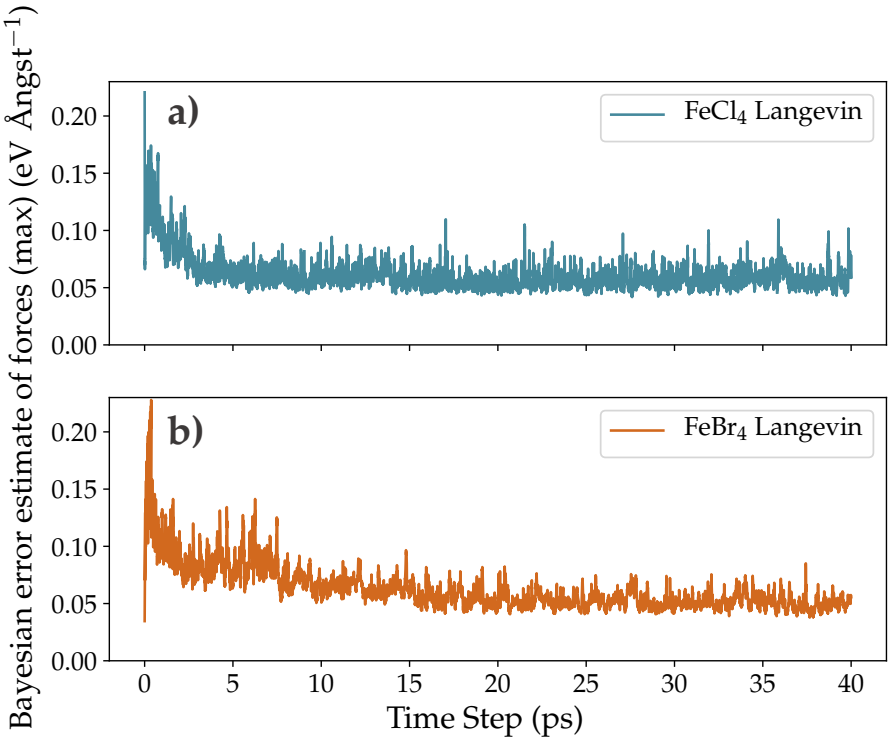

Figure D.1: Bayesian error estimate of forces (BEEF) for the generation of machine learned force fields (MLFF) from 200 K to 200 K for the two plastic crystals.

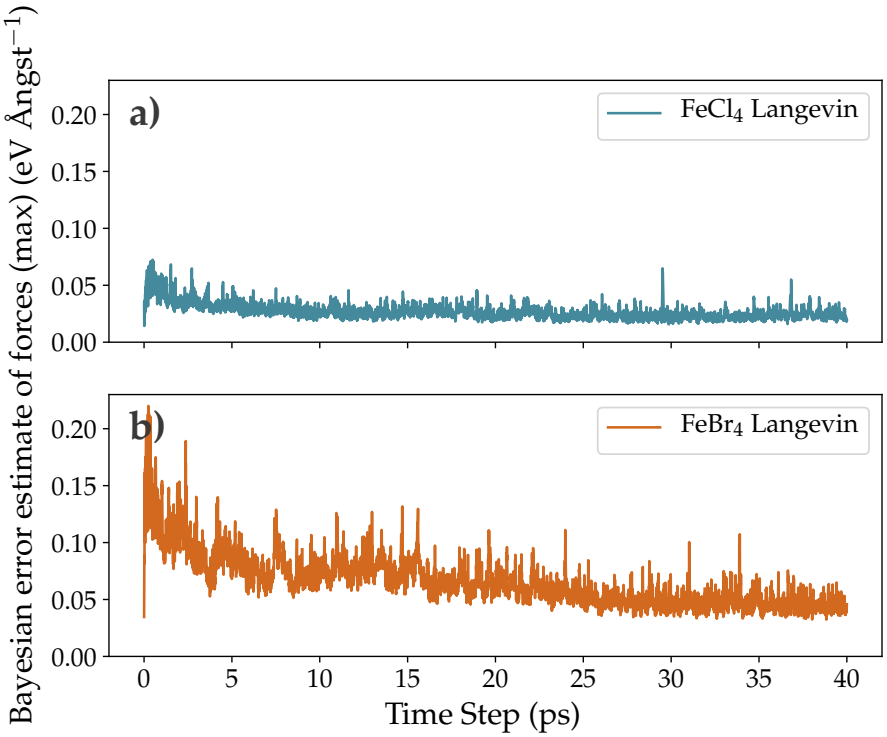

Figure D.2: Bayesian error estimate of forces (BEEF) for the generation of machine learned force fields (MLFF) from 400 K to 400 K for the two plastic crystals.

E

NOSÉ-HOOVER TEMPERATURE AND TOTAL ENERGY

Figure E.1, E.2 and E.3 gives the temperature and energy per atom for the constant volume calculations using the Nosé-Hoover thermostat at 200 K, 300 K and 400 K.

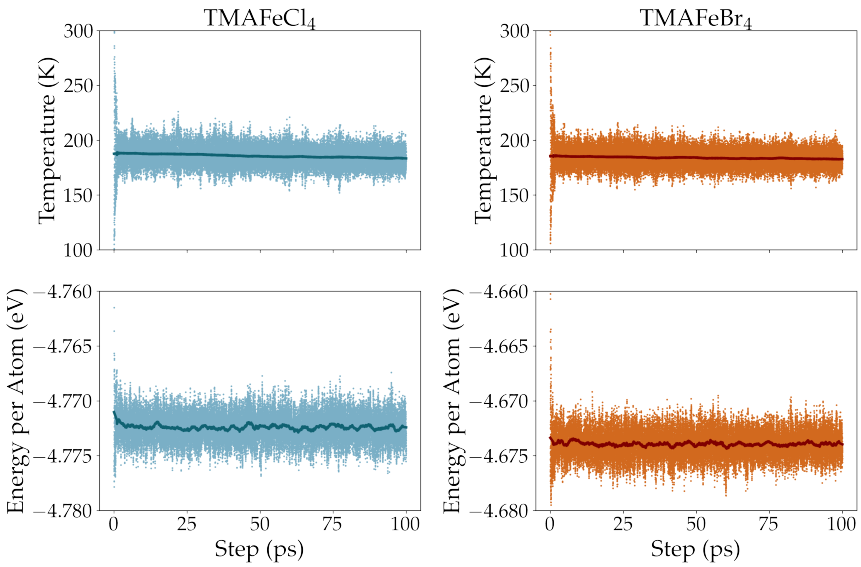

Figure E.1: Energy and temperature for the Nosé-Hoover calculation from 200 K to 200 K.

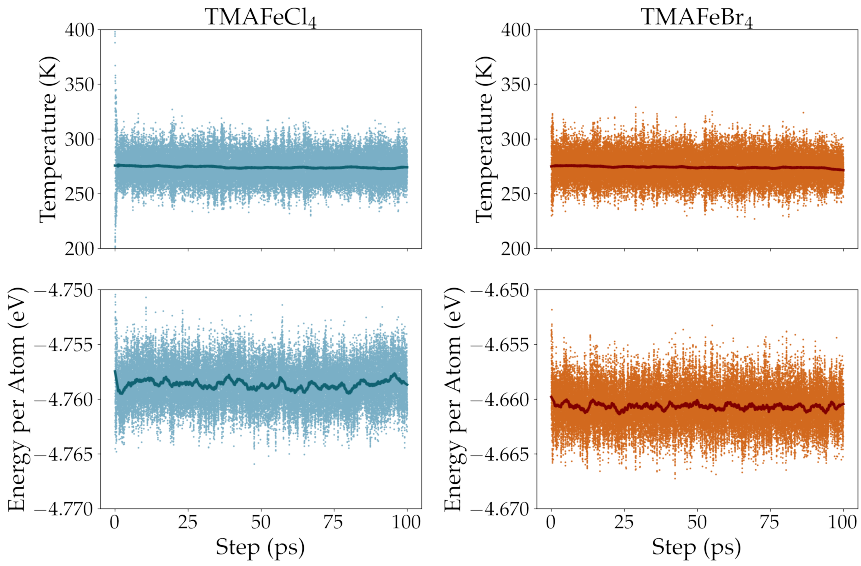

Figure E.2: Energy and temperature for the Nosé-Hoover calculation from 300 K to 300 K.

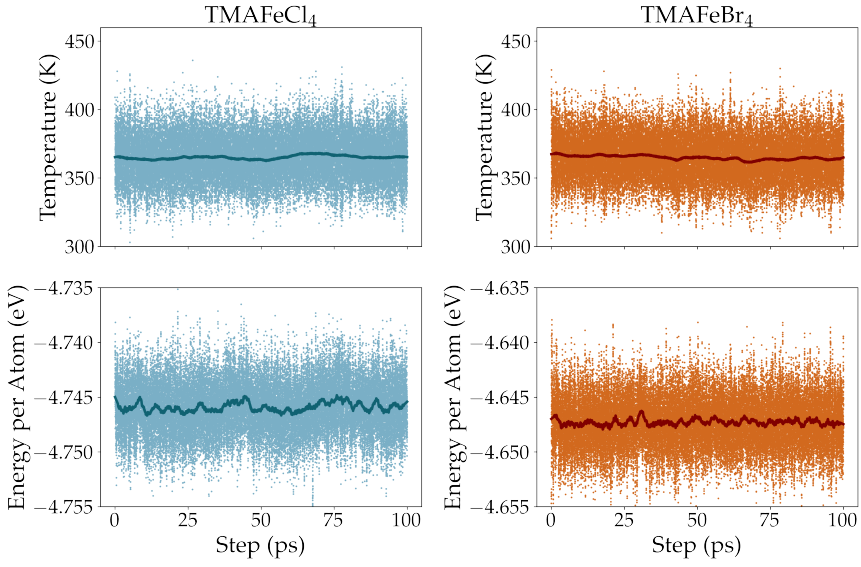

Figure E.3: Energy and temperature for the Nosé-Hoover calculation from 400 K to 400 K.

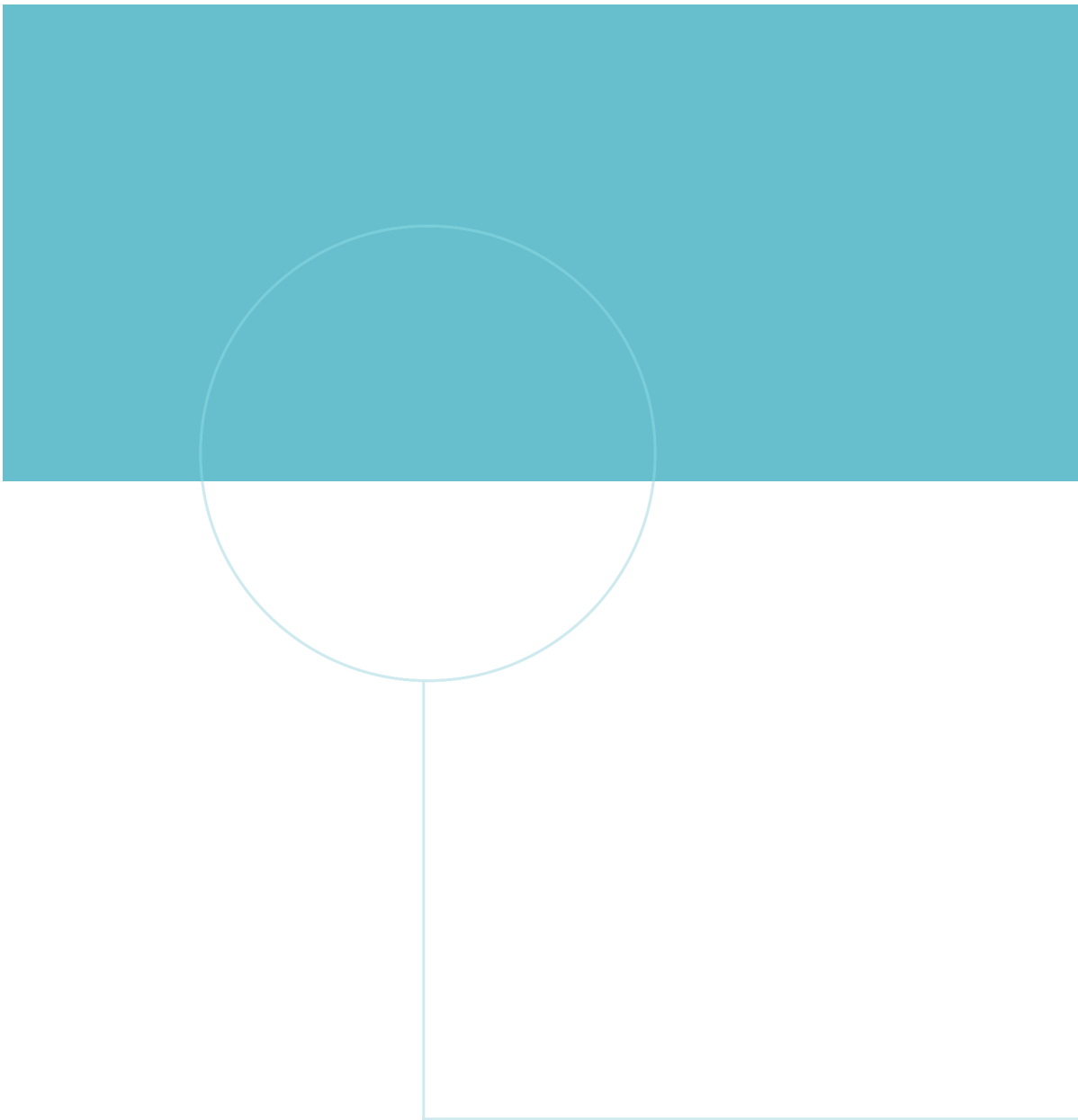

NTNU

Norwegian University of
Science and Technology